AIAA Journal
Vol. 55, No. 10, October 2017

Effect of Weak Outlet-Guide-Vane Heterogeneity on Rotor–Stator Tonal Noise

Marlène Sanjosé* and Stéphane Moreau†
Université de Sherbrooke, Sherbrooke, Quebec J1K 2R1, Canada
and
Miguel Pestana‡ and Michel Roger§
École Centrale de Lyon, 69134 Écully, France

DOI: 10.2514/1.J055525

Four numerical simulations of the NASA Active Noise Control Fan rig with some modifications have been performed to investigate the influence of the heterogeneity of the stator row on the tonal noise radiation for a realistic turbofan with a high hub-to-tip ratio. These simulations achieved with the Powerflow solver based on the lattice Boltzmann method provide a direct acoustic prediction for both tonal and broadband noise. The numerical simulations are used to evaluate the noise contributions of the rotor-wake interaction with the stator vanes, and the rotor interaction with both the inlet distortion and the potential field generated by the stator row. Analytical models are evaluated on this configuration using the flow description provided by the simulations. Rotor-wake and inlet-distortion interaction noise generation with in-duct propagation uses the classical Amiet's response, whereas Parry's model is used for the rotor response to the potential field. The simulation is used to evaluate simple excitation models for the potential field and the rotor-wake evolutions. The analytical results for homogeneous and heterogeneous configurations compare well with the detailed acoustic modal powers extracted from the direct acoustic field simulated with Powerflow. The wake interaction remains the dominant source in the present heterogeneous configurations.

Nomenclature

$\mathcal{A}$	=	amplitude of g [see Eq. (9)]
a, b	=	ellipse parameters
a_m, b_m	=	interpolation parameters
B	=	number of rotor blades
$\mathcal{B}$	=	phase angle from duct to profile coordinates
b	=	blade/vane half-chord
C_R, C_S, C_{MS}	=	blade, vane, and modified vane chord, respectively
c_0	=	speed of sound
$d_{R/S}$	=	rotor–stator distance
E	=	Fresnel integral
E_{nj}	=	duct radial function
ES, Es	=	modified Fresnel functions
$\boldsymbol{e}_r, \boldsymbol{e}_\theta, \boldsymbol{e}_x$	=	cylindrical unit vectors
F_m	=	Fourier coefficient of the upwash velocity
F_T, F_D	=	axial and tangential lift components, respectively
$\boldsymbol{f}$	=	force exerted by the blade/vane surface S on the fluid
$f(M)$	=	function to account for the compressibility effects at high frequency in the Sear's response
G	=	annular duct Green's function
g	=	normalized pressure jump
J_n	=	Bessel function of the first kind of order n
j	=	radial order of the duct mode (n, j)
K	=	conformal mapping parameter
$\mathcal{K}$	=	convective wave number [see Eq. (9)]
k	=	vane summation index
k_c	=	complex aerodynamic wave number
k_d	=	damping coefficient
k_m	=	gust acoustic wave number
k_x, k_y	=	streamwise and normal aerodynamic wave number, respectively
k_0	=	acoustic wave number
l	=	unsteady lift function
M_a	=	mean duct axial Mach number
M	=	local Mach number
m	=	loading harmonic index
N_{nj}	=	coefficient of duct radial function
N_{nj}	=	amplitude in duct mode shape function
n	=	azimuthal order of the duct mode (n, j)
P	=	aerodynamic unsteady pressure
p	=	acoustic pressure
q	=	parameter of the conforming mapping
$\mathcal{R}_d(r, \theta, x)$	=	cylindrical reference frame (fixed to the duct)
R_H, R_T	=	hub and tip duct radius, respectively
S	=	radial cut perimeter
$\mathcal{S}$	=	Sears's function
$\mathcal{S}$	=	blade surface
s	=	blade-passing frequency index
T	=	time period
T_{bpp}	=	blade-passing period
T_q	=	conformal mapping
T_{nj}, D_{nj}	=	modal coefficients of loading components (axial and tangential, respectively)
t, τ	=	observer and emission time, respectively
U, U_c	=	freestream and convection speed, respectively
u_{pot}	=	upwash velocity
$\hat{u}_{\mathrm{abs}}$	=	Fourier coefficient of absolute velocity
V	=	number of stator vanes
w_0	=	gust amplitude
w_m	=	aerodynamic gust of loading harmonic m
$\boldsymbol{x}$	=	(r, θ, x) observer position in $\mathcal{R}_d$ reference frame
$\boldsymbol{x}'$	=	(r', θ', x') source position in $\mathcal{R}_d$ reference frame
x_0	=	source plane localization
(x_c, y_c)	=	blade/vane Cartesian coordinate system
Y_n	=	Bessel function of the second kind of order n
z	=	complex number

Received 19 July 2016; revision received 14 March 2017; accepted for publication 4 April 2017; published online 27 June 2017.

*Researcher, Mechanical Engineering Department; marlene.sanjose@usherbrooke.ca.
†Professor, Mechanical Engineering Department. Lifetime Member AIAA.
‡Ph.D. Student, LMFA.
§Professor, LMFA.

β	=	compressibility parameter
β, β_a	=	compressibility parameters based on M and M_a, respectively
Γ_{nj}	=	duct radial function normalization factor
θ_i $(i = 1, 4)$	=	constants in radiation integrals
γ_{nj}	=	axial wave number
κ_{nj}	=	cutoff criterion
λ	=	wavelength
μ	=	frequency parameter
τ_{nj}	=	phase angle in duct mode shape function definition
ρ_0	=	fluid density
$\Phi[z]$	=	complex error function of argument z
φ_0	=	modified acoustic potential solution to the Helmholtz equation
χ_{nj}	=	duct eigenvalues
$\chi_R, \chi_S, \chi_{MS}$	=	blade, vane, and modified vane stagger angle
Ω	=	engine rotational speed, rad/s
ω	=	acoustic angular frequency
ω_m	=	gust angular frequency

Subscripts

n	=	azimuthal mode order
j	=	radial mode order

Superscripts

$\pm$	=	downstream and upstream propagation
$-$	=	made nondimensional by b
$\star$	=	Fourier conjugate
δ	=	relative to potential effect

I. Introduction

TO REDUCE pollutant emissions and fuel consumption, future turbofan architectures will have increased bypass ratio and reduced size of the nacelle. The advantage of such engines is to reach the necessary thrust at takeoff with a smaller fan rotational speed. In terms of acoustic emission, it is changing the relative contribution of noise sources; in particular, the interaction of the rotor wakes with the outlet guiding vanes (OGVs) becomes dominant especially because the fan OGV distance is reduced. Furthermore, structural components are included in the stator row, yielding a heterogeneity that generates stronger upstream distortions and induce additional noise sources on the fan itself. Noise prediction tools based on analytical models must be improved to account for these new challenges.

The present work addresses a simplified but representative configuration to isolate the effect of the heterogeneity of the OGV on tonal noise sources. It mostly focuses on the potential field distortion interacting with the rotor and compares it with the rotor–stator wake interaction that has been more intensively studied by de Laborderie et al. [1–3], Holewa et al. [4], and more recently Bonneau et al. [5] and Daroukh et al. [6], for instance. Compared with the last three studies, the present heterogeneity does not involve massive bifurcations that create strong flow modifications in the blades passages so that the various noise sources could be more easily separated. The baseline configuration of the NASA Active Noise Control Fan (ANCF) test rig is used as a reference case typical of a low-speed high-bypass-ratio turbofan. The ANCF has been intensively studied at the Aeroacoustic Propulsion Laboratory facility at NASA Glenn Research Center. Measurements have been performed on various stage configurations and flow conditions, yielding a large aerodynamic and acoustic database [7–9]. Therefore, this low hub-to-tip ratio axial fan stage provides an excellent test bed for aeroacoustic code validation of ducted turbomachines with significant modal content. Moreover, the relatively low Mach number of the ANCF allows comparing various numerical approaches, solving either the Navier–Stokes equations [10] or the Boltzmann equations for the gas dynamics. Detailed three-dimensional (3-D) turbulent compressible unsteady simulations have been recently performed on two configurations of this fan stage using a lattice Boltzmann method (LBM) particularly adapted to low Mach numbers [11–13]. These simulations including the full geometry of the installation were shown to accurately reproduce the acoustic measurements made in the anechoic facility. They complement the experimental database by possibly providing a direct insight into the aerodynamic sources (mainly the rotor wakes impinging on the stator) in addition to the in-duct and far-field direct acoustic propagation.

From the baseline LBM simulation with a homogeneous stator row, a heterogeneous configuration is built by enlarging a single stator vane, keeping the profile definition and blade stacking identical. For the same operating condition, the heterogeneous configuration allows isolating the influence of the potential effect of the stator row limiting the strong modification of flow structure in the machine. This case is intensively used to calibrate and validate analytical methods used for the noise predictions of realistic turbofans.

The numerical setups of the homogeneous and heterogeneous configurations are described in Sec. II. The aeroacoustic models for tonal noise are described in Sec. III. The analytical and numerical excitation models as well as the unsteady blade loading are studied in Sec. IV, and the acoustic predictions based on analytical and numerical approaches are compared in Sec. V.

II. Numerical Simulation of a Simplified Heterogeneous Configuration

The present simulations use the Powerflow solver 5.0a based on the lattice Boltzmann method (LBM). The approach is naturally transient and compressible, providing a direct insight into hydrodynamic mechanisms responsible for the acoustic emission but also into acoustic propagation in the nacelle and outside in the free field.

Instead of studying macroscopic fluid quantities, the LBM tracks the time and space evolution on a lattice grid of a truncated particle distribution function. The particle distribution evolution is driven to the equilibrium by the so-called collision operator, approximated by the Bhatnagar–Gross–Krook model. The discrete lattice Boltzmann equations need to be solved for a finite number of particle velocities. The discretization retained in Powerflow involves 19 discrete velocities for the third-order truncation of the particle distribution function, which has been shown sufficient to recover the Navier–Stokes equations for a perfect gas at low Mach number in isothermal conditions [14–16]. In Powerflow, a single relaxation time is used, which is related to the dimensionless laminar kinematic viscosity [17]. This relaxation time is replaced by an effective turbulent relaxation time that is derived from a systematic renormalization group procedure detailed in Chen et al. [18]. It captures the large structures in the anechoic room (included in the computational domain) but also the small turbulent scales that develop along the blade and duct surfaces where wall-law boundary conditions accounting for pressure gradients are applied using specular reflections [19]. The particular extension of the method developed for rotating machines can be found in Zhang et al. [20].

With this method, the flowfield is computed on the full test rig of the Aero-Acoustic Propulsion Laboratory at NASA Glenn Research Center [7–9]. Only the rotor driving system and the measurement system are not considered in the setup. A detail of the ducted fan is shown in Fig. 1. The actual laboratory is also replaced by a very large anechoic room of dimensions $132 \times 113 \times 113$ m to mimic the actual experimental setup and to include damping zones around it. The present full setup is similar to the one used in previous studies [11,12]. The configuration includes the 1.22-m-diam duct with the precise geometry for the bell mouth and the hub. The study focuses on the nominal fan conditions; the fan has $B = 16$ blades and is rotating at 1800 rpm. The tip clearance of 0.05% fan diameter is ignored by extruding the blades to the duct. The finest grid resolution around the rotor and stator is 0.1% fan diameter and 0.2% fan diameter in the interstage space. The refinement is not sufficient to capture all turbulent scales, as shown in a previous study [13], but it is sufficient

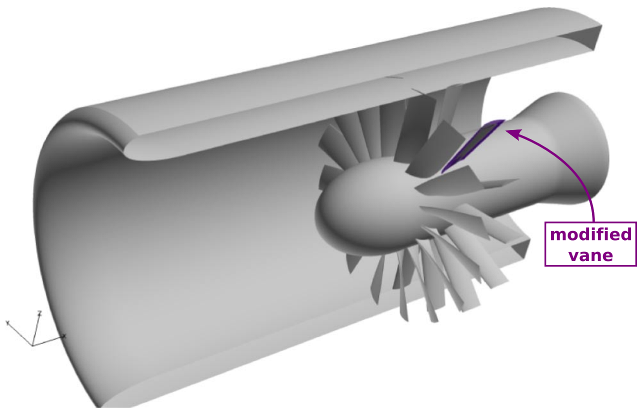

Fig. 1 Simulated geometry with half the nacelle hidden for visualization purpose. The modified vane is highlighted in purple.

to capture the deterministic interactions between the rotor and the stator and to propagate acoustic waves within the nacelle up to the third blade-passing frequency (BPF) harmonic thanks to the very low-dissipation properties of the LBM numerical method. With this model, converged results are obtained within three weeks using 288 processors allowing some parametric studies at a reasonable cost. In the present work, two stator configurations have been investigated to isolate the effect of the stator heterogeneity. The rotor–stator distance $d_{R/S} = 0.5C_R$ is measured at the hub and given in terms of rotor chord C_R. Two OGV configurations are investigated with a vane count of $V = 14$ or 26 respectively. The comparison of the two setups allows investigating the heterogeneity impact on the first blade-passing frequency, which is cut on in the homogeneous configuration with $V = 14$ vanes and cut off in the homogeneous configuration with $V = 26$ vanes. In the homogeneous configuration, all vanes are identical, whereas in the heterogeneous configuration, one single vane is scaled up by a factor 1.5, keeping the leading-edge aligned with all other vanes. For the four simulations, the same mesh refinement zones are used based on the work of Mann et al. [11]. The simulation time step is 2.44×10^{-6} s. A transient time of 10 fan rotations is observed for all configurations; then, volume measurements are recorded in a volume around the rotor–stator stage 26 times per blade-passing period $T_{\mathrm{bpp}} = 2\pi/B\Omega$, yielding a sampling frequency of 12,480 Hz. Additional axial extraction planes are recorded upstream of the rotor row, in the middle of the rotor–stator interstage, and downstream of the OGV with a smaller sampling period of $T_{\mathrm{bpp}}/123$ corresponding to a sampling frequency of 59,040 Hz to extract the upstream distortion, the velocity deficit in the rotor wakes, and the acoustic power in the duct.

III. Aeroacoustic Analytical Models

The rotor/stator is mounted in an infinite annular duct of constant section. The cylindrical reference frame $\mathcal{R}_d(r, \theta, x)$ is fixed to the duct with its axial direction corresponding to the machine axis oriented toward the exhaust of the duct.

For the implementation of analytical models, the true blades and vanes are simplified to flat plates extruded over the radial direction. The blades and vanes are divided into 19 strip elements on which neither sweep nor lean are considered, and the chord C and stagger angle χ defined from the machine axis are assumed constant over the strip heights. This so-called strip theory allows to capture the main variations of geometry and flow parameters over the duct section. The parameters extracted from the ANCF geometry at midspan are given in Table 1.

For the acoustic propagation, with the rotational speed of the machine being low, the swirl effects are ignored [21]. Only an inviscid mean axial flow of Mach number M_a is considered. Within these assumptions, Goldstein's analogy [22] provides the acoustic pressure in the duct resulting from the force $\boldsymbol{f}$ exerted by the blade surface S on the fluid using the annular duct Green's function G, the expression of which is provided in the frequency domain in Appendix A:

$$p(\boldsymbol{x}, t) = \int_{-T}^{T} \iint_{\mathcal{S}(\tau)} \frac{\partial G(\boldsymbol{x}, t|\boldsymbol{x}', \tau)}{\partial x_i'} f_i(\boldsymbol{x}', \tau)\, \mathrm{d}S(\boldsymbol{x}')\, \mathrm{d}\tau \tag{1}$$

where T is a large but finite time period sufficient to capture all the aerodynamic effects on the sound; τ and t are the emission and reception times; and $\boldsymbol{x}'$ and $\boldsymbol{x}$ are the source and observer positions, respectively, in the duct coordinate system.

Neglecting the radial component of the force, the latter can be decomposed as a thrust (axial) component and a drag (tangential) component, $\boldsymbol{f} = F_D \boldsymbol{e}_\theta + F_T \boldsymbol{e}_x$, that are related to the unsteady lift l: $F_D = \mathrm{sign}(\chi) l(x_c) \cos(\chi)$ and $F_T = \mathrm{sign}(\chi) l(x_c) \sin(\chi)$, with the force on the blade pointing toward the suction side. Because of the low counts of rotor blades and stator vanes, an isolated airfoil response model is used to compute the pressure jump.

A. Homogeneous Rotor Row

For the rotor with B identical blades experiencing a periodic excitation over a revolution, the acoustic pressure due to the potential distortion can be expressed at a given harmonic of the blade-passing frequency ($\omega = sB\Omega$) as

$$p_{sB}(\boldsymbol{x}) = \frac{B}{2} \sum_{n=-\infty}^{+\infty} \sum_{j=1}^{+\infty} \frac{E_{nj}(r)}{\Gamma_{nj}\kappa_{nj}} \mathrm{e}^{i(n\theta - \gamma_{nj}^{\pm} x)} \times (nD_{nj}^{\pm} - \gamma_{nj}^{\pm} T_{nj}^{\pm}) \tag{2}$$

with the modal coefficients $D_{nj}^{\pm}$ and $T_{nj}^{\pm}$ defined as the integration of the lift weighted by a noncompactness phase shift over the blade surface. After a change of variable to make the abscissa dimensionless with the half-chord $\overline{x}_c = x_c/b$ and neglecting phase angles (that do not contribute to the acoustic power in the present single-strip approximation), $D_{nj}^{\pm}$ and $T_{nj}^{\pm}$ can be written as

$$\begin{aligned} D_{nj}^{\pm} &= (R_T - R_H) E_{nj}(r') \frac{b}{r} \int_{-1}^{1} \mathrm{e}^{-i\mathcal{B}\overline{x}_c} l(\overline{x}_c) \sin(\chi)\, \mathrm{d}\overline{x}_c \\ T_{nj}^{\pm} &= (R_T - R_H) E_{nj}(r') \frac{b}{r} \int_{-1}^{1} \mathrm{e}^{-i\mathcal{B}\overline{x}_c} l(\overline{x}_c) \cos(\chi)\, \mathrm{d}\overline{x}_c \end{aligned} \tag{3}$$

where the phase angle $\mathcal{B} = b(\gamma_{nj}^{\pm} \cos\chi - (n/r') \sin\chi)$ comes from the wave number expressed in the blade Cartesian coordinates.

By integrating the expression of the acoustic intensity originally proposed by Cantrell and Hart over the duct section, the upstream and downstream acoustic powers are written as

$$\Pi^{\pm} = \frac{\pi\beta_a^4 B^2}{2\Gamma_{nj}\rho_0 c_0} \sum_{s=1}^{\infty} \sum_{n=-\infty}^{+\infty} \sum_{j=0}^{\infty} \frac{sB\Omega |nD_{nj}^{\pm} - \gamma_{nj}^{\pm} T_{nj}^{\pm}|^2}{\kappa_{nj}(sB\Omega/c_0 \pm \kappa_{nj} M_a)^2} \tag{4}$$

with $\beta_a = \sqrt{1 - M_a^2}$ [22–24].

Table 1 Geometrical parameters of the rotor–stator stage

Row	Blade/vane number	Chord, cm	Stagger angle, deg	Solidity (chord/blade gap)
Rotor	$B = 16$	$C_R = 13.4$	$\chi_R = -53.7$	0.86
Stator	$V = 14$ or 26	$C_S = 11.5$	$\chi_R = 9.9$	0.65 or 1.20
Modified vane	— —	$C_{\mathrm{MS}} = 17.3$	$\chi_{\mathrm{MS}} = 9.6$	— —

B. Heterogeneous Stator Row

For the stator, each vane is submitted to a periodic excitation from the rotor wakes. The pressure from the rotor–stator interaction can be expressed at the harmonic of the blade-passing frequency $sB\Omega$ as a sum over all stator vanes:

$$p_{sB}(\boldsymbol{x}) = \frac{1}{2}\sum_{n=-\infty}^{+\infty}\sum_{j=1}^{+\infty}\frac{E_{nj}(r)}{\Gamma_{nj}\kappa_{nj}}\mathrm{e}^{i(n\theta-\gamma_{nj}^{\pm}x)} \times \sum_{k=0}^{V-1}\mathrm{e}^{ik(sB-n)(2\pi/V)}(nD_{nj,k}^{\pm}-\gamma_{nj}^{\pm}T_{nj,k}^{\pm}) \tag{5}$$

where the double sum is limited to the acoustic duct modes (n,j) excited by the rotor–stator interaction following the extended Tyler and Sofrin's rule [5,25,26]:

$$\mathrm{sign}(\Omega)sB - n = m \quad \text{with: } m\in\mathbb{Z} \tag{6}$$

with the same expression for $D_{nj,k}^{\pm}$ and $T_{nj,k}^{\pm}$ as in Eq. (3), accounting for the specific half-chord b_k and stagger angle χ_k of each vane.

In the previous expressions, the remaining terms to be calculated are the loadings of the blades/vanes, detailed in the next sections.

C. Amiet's Blade/Vane Response

The lift response function for an airfoil in rectilinear motion to a harmonic gust at the angular frequency $\omega_m = m\Omega$, with m the loading harmonic index defined by

$$w_m = w_0\mathrm{e}^{i(k_x x_c + k_y y_c - \omega_m t)} \tag{7}$$

is given as the conjugate of the expression provided by Amiet [27], accounting only for gusts parallel to the leading edge:

$$l(\overline{x}_c) = 2\pi\rho_0 U w_0 g^{\star}(\overline{x}_c, \overline{k}_x, 0, M) \tag{8}$$

where $g^{\star}$ is the normalized pressure jump given in Appendix B ($\star$ denotes the conjugate required because of a different convention in the Fourier transform). U_c is the convection velocity of the gust assumed to be equal to the freestream velocity U in the reference frame of the blade; $\overline{k}_x = \omega_m b/U$ the dimensionless axial wave number; $\overline{\mu} = bk_m/\beta^2$, where $k_m = \omega_m/c_0$ is the acoustic wave number of the gust; and M is the local Mach number seen by the airfoil. The overbar defines a variable made dimensionless by the half-chord.

This model is applied for rotor-wake interaction on the homogeneous and heterogeneous stator rows under the assumption that the cascade effect is negligible.

D. Parry's Blade Response

The response of a blade due to a potential perturbation from downstream is modeled in this section. In the case of small enough rotor–stator spacings, the potential field in the upstream vicinity of stator vanes is seen as a downstream distortion by the rotor blades. This interaction cannot be modeled by the classical Amiet's theory because it represents a contamination at the trailing edge instead of at the leading edge. Moreover, the amplitude of the velocity perturbation decreases going upstream, as opposed to a classical unsteady-aerodynamics approach, where a frozen disturbance is convected downstream by the flow. Previous studies [28] have modeled this interaction noise by a reversed Amiet's resolution formulated on the potential ignoring the Kutta condition. The modeling is readdressed here with the approach presented in Parry's dissertation [29]. A boundary-value problem is formulated on the pressure imposing the Kutta condition and considering a complex hydrodynamic wave number to reproduce the potential decrease. The Kutta condition imposes a zero pressure jump at the trailing edge. The velocity upwash seen by the rotor blades is described using the same convention as previously defined in Eq. (7).

The axial wave number is now defined as $k_c = k_x + ik_d$. k_x is the classic hydrodynamic wave number of the gust, and k_d corresponds to a damping factor. The velocity potential associated with the blade response satisfies a convected wave equation that is solved analytically on an infinite flat plate on which the rigidity condition is imposed. Parry [29] uses a Wiener–Hopf technique to solve the convected Helmholtz equation with boundary conditions. When the Kutta condition is not imposed, the pressure jump is singular at the trailing edge. Parry removes the singularity by means of a vortex sheet. Here, the Kutta condition is intrinsic to the formulated problem. An equivalent approach is adopted by solving the previous system with Schwarzschild's technique [30,31]. When applied to finite-chord airfoils, this method is based on the iterative solving of half-plane problems, considering alternatively semi-infinite flat plates extending upstream or downstream from the trailing edge or the leading edge.

The first approximation is solved in two subiterations with subscripts 0 and 1. The first one consists of applying the rigidity condition to an artificial infinite flat plate. The solution $\varphi_0(\overline{x}_c, 0)$ of this first subiteration can then be related to the pressure by

$$P_0 = -\rho_0 U w_0 \mathcal{A}\mathrm{e}^{i\overline{k}_c(\overline{x}_c-1)} \quad \text{with } \mathcal{A} = \frac{i\overline{k}_d}{\beta\sqrt{\overline{\mu}^2 - \overline{\mathcal{K}}^2}} \tag{9}$$

where $\overline{\mathcal{K}} = \overline{k}_c + M\overline{k}_m/\beta^2$.

Then, a new Amiet–Schwarzschild boundary-value problem is formulated on the additional pressure P_1 that is needed to satisfy the Kutta condition for the total pressure written $P = P_0 + P_1$. The solution for the additional pressure is then given by

$$P_1(x,0) = \rho_0 U w_0 \mathcal{A}\mathrm{e}^{i\overline{k}_c(\overline{x}_c-1)}\left[1 - \Phi\left[\sqrt{i(\overline{\mu}+\overline{\mathcal{K}})(\overline{x}_c-1)}\right]\right] \tag{10}$$

where Φ is the complex error function for complex arguments [32].

For the case of a flat plate, oscillations at the trailing-edge are considered to be in phase opposition, which allows to express the unsteady lift as two times the pressure $l = 2P$. This leads to the final unsteady load expressed in terms of the dimensionless coordinate $\overline{x}_c$:

$$\begin{aligned} l^{\Delta}(\overline{x}_c, 0) &= 2P(\overline{x}_c, 0) = 2[P_0(\overline{x}_c, 0) + P_1(\overline{x}_c, 0)] \\ &= 2\rho_0 U w_0 g^{\Delta}(\overline{x}_c, \overline{k}_c, 0, M) \end{aligned} \tag{11}$$

with

$$g^{\Delta}(\overline{x}_c, \overline{k}_c, 0, M) = -\mathcal{A}\mathrm{e}^{i\overline{k}_c(\overline{x}_c-1)}\Phi\left[\sqrt{i(\overline{\mu}+\overline{\mathcal{K}})(\overline{x}_c-1)}\right] \tag{12}$$

In Fig. 2, the pressure jump according to the reversed Sears's theory [28] is compared with the present formulation that accounts for the Kutta condition. The additional singular term present when the Kutta condition is not applied is responsible for an increase in the pressure jump over the whole chord length and for the singularity at the trailing edge. Otherwise, when the Kutta condition is applied, the pressure jump is correctly canceled at the trailing edge, and the present formulation exactly fits with Parry's Wiener–Hopf derivation. In both models, as expected for this kind of interaction,

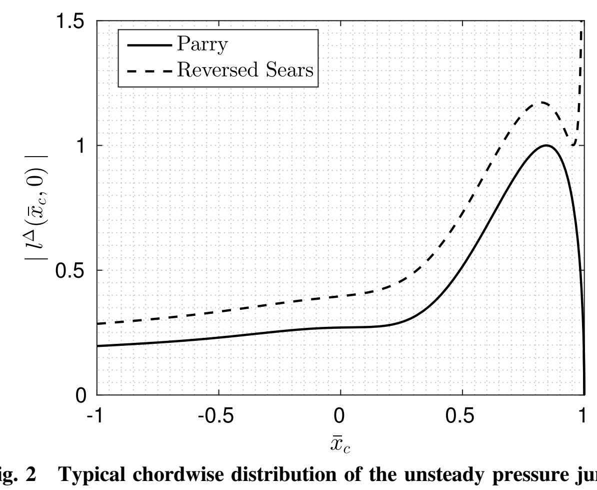

Fig. 2 Typical chordwise distribution of the unsteady pressure jump amplitude according to analytical models.

the unsteady loading concentrates in the trailing-edge region and strongly decreases in the upstream direction.

This iteration is a good approximation at high frequencies for which the source is not compact, $2b \gg \lambda$ (where λ is the wavelength). To extend the model, a further leading-edge correction (second Amiet–Schwarzschild iteration) should be carried out. This is not addressed in the present work.

The pressure jump is finally introduced in the radiation integral in Eq. (3). After some derivations, the chordwise integral is found as

$$\begin{aligned}\mathcal{L}^{\Delta} \equiv &= \int_{-1}^{1} \mathrm{e}^{-i\mathcal{B}\bar{x}_c} l^{\Delta}(\bar{x}_c)\,\mathrm{d}\bar{x}_c \\ &= -2\rho_0 U w_0 \mathcal{A} \frac{(1+i)\mathrm{e}^{-i\mathcal{B}}}{\Theta_3} \left\{ i\mathrm{e}^{-2i\Theta_3} E^{\star}[-2\boldsymbol{i}\Theta_4] \right. \\ &\quad \left. - i\sqrt{\frac{\Theta_4}{\Theta_4 - \Theta_3}} E^{\star}[-2(\Theta_4 - \Theta_3)] \right\} \end{aligned} \tag{13}$$

where $\Theta_3 = \bar{k}_c - \mathcal{B}$, and $\Theta_4 = (\bar{\mu} + \bar{\mathcal{K}})$. The parameters w_0 and k_d of the gust are investigated in the next section.

This model adapted for trailing-edge interactions is formulated in a way similar to Amiet's airfoil response and under the assumption of a negligible cascade effect. This effect could be added in a future work following the methodology developed for the trailing-edge noise [33]. In the case of rotor excitation by nonidentical stator vanes, the heterogeneity is introduced in the expression of the gust through the value of w_0.

All the models presented in this section are available in the analytical noise prediction code OPTIBRUI developed in the framework of an industrial consortium.

IV. Excitation Models

A. Analytical Models for the Potential Field

The modeling of the potential field can be achieved with the classical potential theory or by extracting computational fluid dynamics (CFD) data.

Potential inviscid theories for two-dimensional flows are investigated here. Using a conformal mapping, the uniform flow around a cylinder in rotation can be transformed into the flow around an isolated airfoil. The mapping reads

$$T_q : z \mapsto z + \frac{q^2}{z} \tag{14}$$

In the present section, three conformal mappings T_q are investigated that transform the cylinder into a flat plate, an ellipse, and a thin Joukowski profile. The parameter q of the conformal mapping and the origin of the complex plane are related to the vane chord, thickness, and camber at each radius [29,34]. The uniform velocity and angle of attack of the flow on the vane are extracted from the numerical simulations in the rotor–stator interstage at each radius. The Kutta condition is ensured by the value of the circulation around the cylinder.

The velocity field for an isolated profile is then duplicated for each vane with a spacing $s = 2\pi r/V$, interpolated on the same grid, and then summed. Compared with the proposed transformation in Appendix 6 of Parry's thesis [29], the present potential field does not include compressibility effects that are presumably negligible in the present configuration.

The velocity of the duplicated potential field is projected along the rotor normal direction $\bar{y}_c$, shown in Fig. 3. (x, y) is a fixed frame of reference with the axial origin placed at the rotor trailing edge and where the origin in y is arbitrary. $(\bar{x}_c, \bar{y}_c)$ is a frame of reference attached to the blade. This upwash velocity u_{pot} is then Fourier transformed in the azimuthal direction $y = r\theta$ in Fig. 3, yielding the excitation seen by the rotor blades at multiples of the rotational frequency:

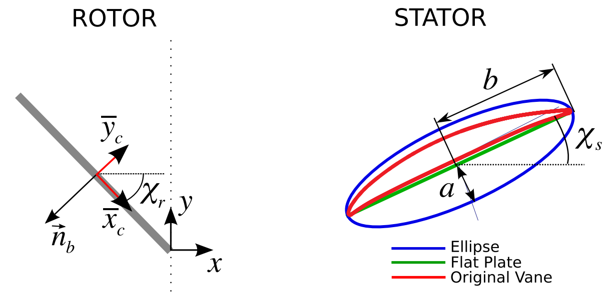

Fig. 3 Geometrical parameters for the computation of the potential effect of the stator.

$$w(x,y) = \sum_{m=-\infty}^{+\infty} F_m(x)\mathrm{e}^{imy(2\pi/S)}$$
$$\text{with } F_m(x) = \frac{1}{S}\int_0^S u_{\mathrm{pot}}(x,y)\mathrm{e}^{-imy(2\pi/S)}\,\mathrm{d}y \tag{15}$$

where $S = 2\pi r$. In general, the Fourier coefficients do not have closed-form expressions and cannot be analytically integrated. For that goal, their decay in the upstream direction is fitted with an exponential axial evolution:

$$w(x,y) = \sum_{m=-\infty}^{+\infty} a_m \mathrm{e}^{b_m x}\mathrm{e}^{imy(2\pi/S)} \tag{16}$$

where a_m and b_m are computed by interpolation for each harmonic order m. This is consistent with the model for potential flow disturbance proposed by Parker [35,36]. Further on, the CFD database will allow analyzing the evolution of the potential upwash velocity and verifying the amplitude and exponential evolution of the coefficients from the three potential theories. Finally, the upwash expression is expressed in a reference frame attached to the rotor blade of coordinates

$$\begin{cases} x = b(\bar{x}_c - 1)\cos\chi_R - \bar{y}_c \sin\chi_R \\ y = b(\bar{x}_c - 1)\sin\chi_R + \bar{y}_c \cos\chi_R \end{cases} \tag{17}$$

A single Fourier component of the upwash gust at $(\bar{x}_c, \bar{y}_c = 0)$ is written

$$\begin{aligned} w_m(\bar{x}_c, 0) &= a_m \mathrm{e}^{i(my(2\pi/S)\sin\chi_R - ib_m\cos\chi_R)b(\bar{x}_c - 1)} \\ &= a_m \mathrm{e}^{i(k_x - ib_m\cos\chi_R)b(\bar{x}_c - 1)} \\ &= w_0 \mathrm{e}^{i\bar{k}_c(\bar{x}_c - 1)} \end{aligned} \tag{18}$$

The parameters of the gust are found by identification: $w_0 = a_m$ and $\bar{k}_c = \bar{k}_x - \boldsymbol{i}b_m\cos\chi_R b$, which leads to a damping factor $\bar{k}_d = -b_m\cos\chi_R b$. Those parameters define the velocity disturbance introduced in Parry's airfoil response model. The Fourier decomposition of the upwash done in this section will be also used with potential fields extracted from CFD simulations in Sec. IV.C for comparison.

B. Identification of the Excitations in the Numerical Simulations

The flow rates for the four simulated configurations are given in Table 2. The difference between the two stator vane numbers is lower than 1%, and the difference between the homogeneous and heterogeneous configurations is almost not noticeable.

This means that the modification of a single vane does not really affect the flow globally. The instantaneous static pressure and axial velocity flowfields on two unwrapped cuts of constant radius are shown in Figs. 4 and 5 for the four simulations. In Fig. 4, the velocity distributions around the rotor blades and the wake deficits at 50% of duct height are not noticeably modified. For the configuration with $V = 14$ vanes, a flow separation is seen at 80% of duct height on the stator suction sides in Fig. 5a. This flow separation is suppressed in the modified vane passage and the preceding one in Fig. 5b. With the solidity being higher in the $V = 26$ configuration, the cascade effect reduces the corner recirculation that cannot be seen anymore at 80% of duct height in Figs. 5c and 5d. Still, the pressure fields shown on the upper part of each field map are noticeably affected by the thickened vane mainly around the stator rows. In the homogeneous

Table 2 Flow rates in the rotor–stator interstage as deduced from the four Powerflow calculations

Configuration	$V = 14$, homogeneous	$V = 14$, heterogeneous	$V = 26$, homogeneous	$V = 26$, heterogeneous
Flow rate, kg/s	54.27	54.27	54.19	54.17

configuration with 14 stator vanes, the pressure patterns around the stator vanes are quite regular at midsection in Fig. 4a. In its heterogeneous version, the pressure patterns from the thickened vane contaminate the neighboring vanes, as shown in Fig. 4b. This is less clear at 80% of duct height because the unsteady detachment on the suction sides modifies the pressure distribution (Figs. 5a and 5b).

In the configuration with 26 stator vanes, the pressure patterns around the stator vanes are also quite regular, but they are affecting each other. A similar pattern with wider spreading is also clearly visible in the heterogeneous configuration in Fig. 4d. Concerning the pressure contours around the rotor blades, no obvious modification by the heterogeneity or the cascade effect could be identified by inspection of Figs. 4 and 5. The setup is thus a relevant test case to isolate the heterogeneity effect on the deterministic rotor–stator interactions at identical flow parameters.

From the result files saved periodically on a volume including the rotor and the stator, the pressure and the absolute velocity are interpolated on a cylindrical regular mesh at several radial locations using the postprocessing python API Antares [37]. The interpolated fields can then be averaged in the rotor or stator reference frame to identify the deterministic excitation of a row by the other one. The phase-locked averages in the rotor and stator reference frames over two full rotor revolutions for the heterogeneous configuration with $V = 14$ are shown in Figs. 6a and 6b, respectively. The cut is performed at midsection of the duct to avoid the contamination by the secondary flows; corner vortices are indeed formed at both vane hub and tip, as already shown by Sanjose et al. [13] (Fig. 4) and Guedeney and Moreau [38] (Figs. 5–8). The analysis is then reduced to two dimensions by unwrapping the cut and neglecting the radial velocity component that is less than 5% of the absolute velocity. Finally, the velocity field is projected on the normal direction to the considered blade and expanded in a Fourier series as explained in Sec. IV.A.

C. Potential Interaction

A comparison between the potential distortion fields predicted by the analytical models and the numerical results is presented in Figs. 7 and 8 for the two heterogeneous stator configurations. Arbitrary levels of the Fourier coefficients F_m are plotted for different harmonic orders m and axial positions between the rotor trailing edge and the stator leading edge.

The first two multiples of the number of vanes V dominate the spectra by 20 dB. However, all orders will contribute to the rotor unsteady lift as shown in Sec. III.A. This results from the modification of one vane, thus breaking the periodicity on the number of stator vanes V. The global surface shape of these excitation spectra is similar in the analytical models and the numerical extraction. For the homogeneous case, not plotted here, the analytical models would only predict tones at the multiples of the number of vanes. For all cases, the 3-D surface

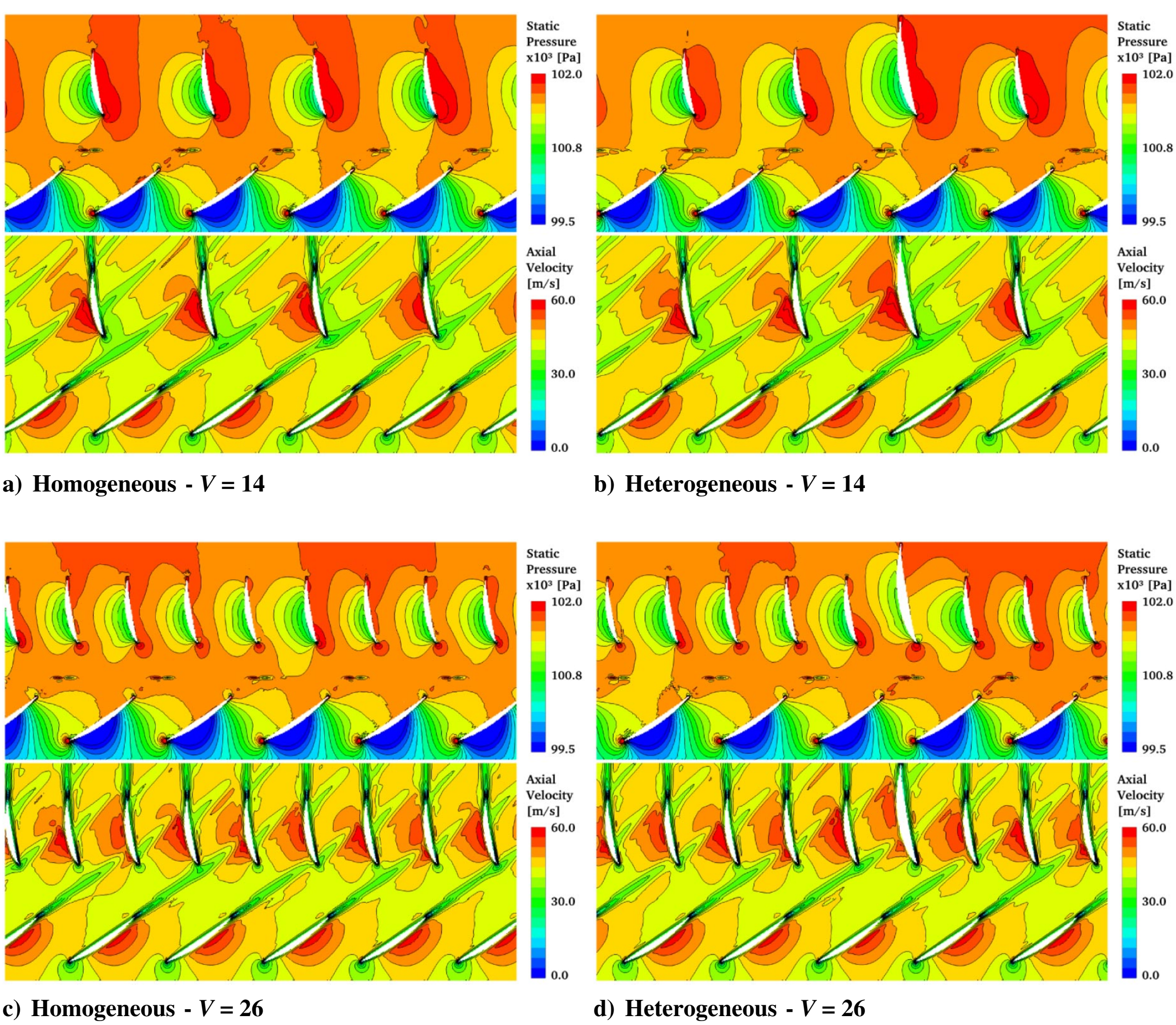

Fig. 4 Instantaneous flowfield in the rotor–stator interstage at 50% of the section height. Static pressure in the upper maps and axial velocity in the lower maps.

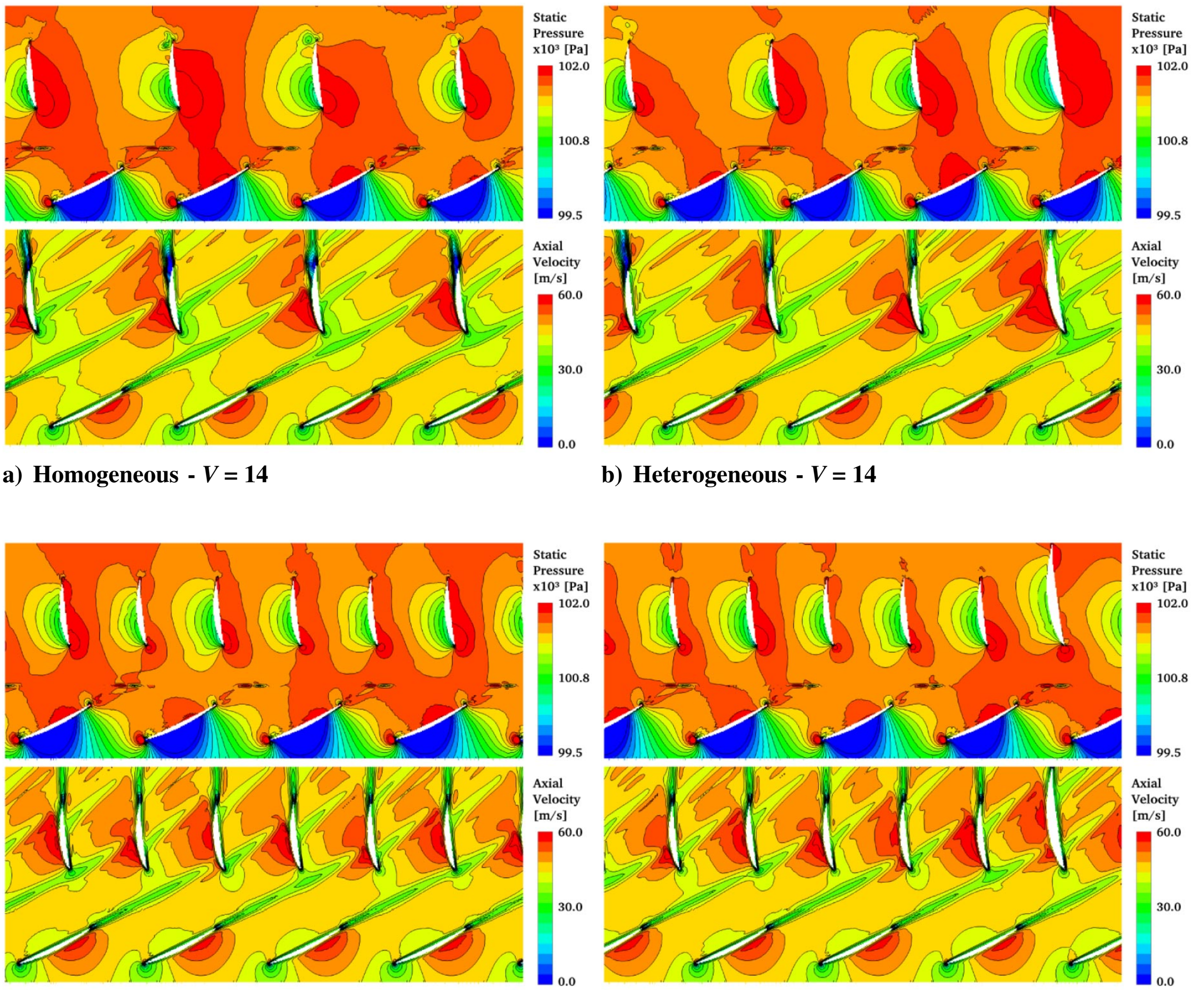

a) Homogeneous - $V = 14$ **b) Heterogeneous - $V = 14$**

c) Homogeneous - $V = 26$ **d) Heterogeneous - $V = 26$**

Fig. 5 Instantaneous flowfield in the rotor–stator interstage at 80% of the section height. Static pressure in the upper maps and axial velocity in the lower maps.

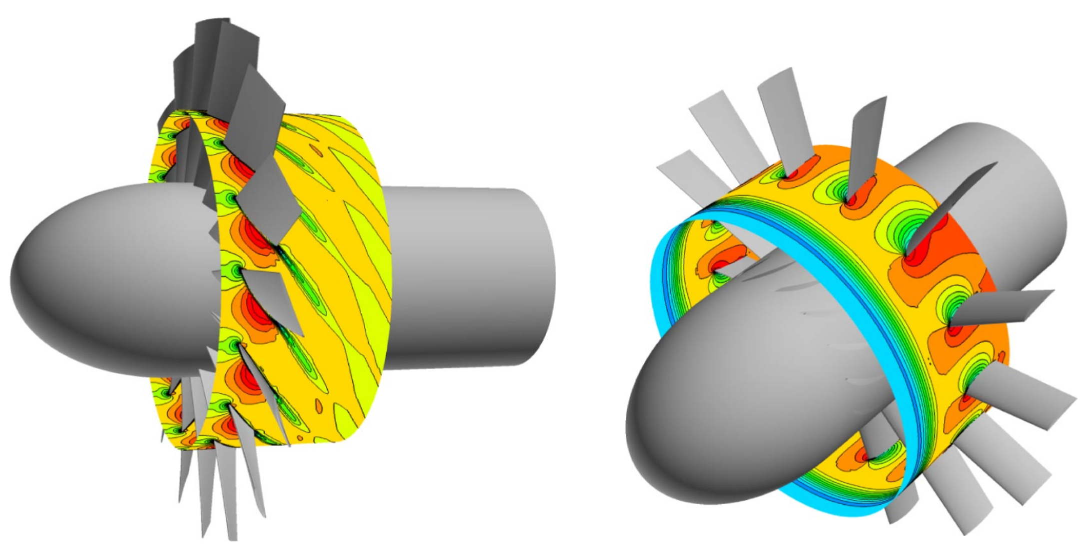

a) Absolute axial velocity field in the rotor reference frame **b) Pressure field in the stator reference frame**

Fig. 6 Phase-locked averages at midsection of the duct for the heterogeneous configuration with $V = 14$.

suggests a nearly exponential decrease with the upstream distance from the stator leading edge. In the numerical extraction, the levels always exceed a background level around −35 dB. This is a numerical artifact from the interpolations and the time convergence of the average. The same behavior is observed in the two stator configurations, with the main harmonic order changing from 14 to 26 due to the different number of vanes. However, Fig. 8c features an additional peak at the harmonic order 38 when approaching the rotor trailing edge

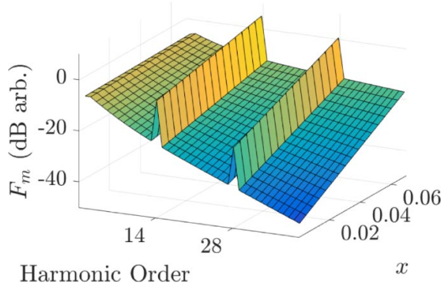

a) Analytical - Ellipses

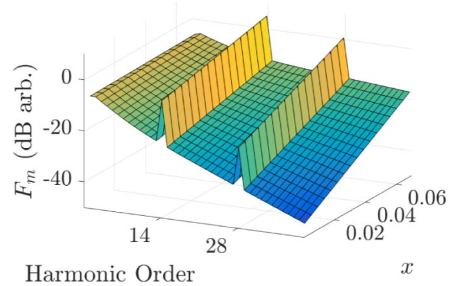

b) Analytical - Flat Plates

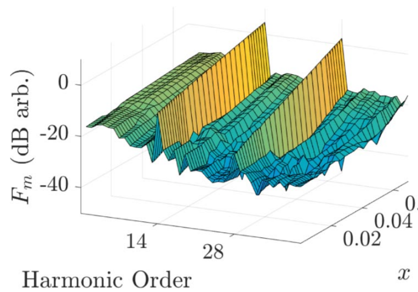

c) Numerical LBM Simulation

Fig. 7 Fourier decomposition of the upwash velocity of the potential distortion for the analytical models and the numerical results in the heterogeneous configuration ($V = 14$).

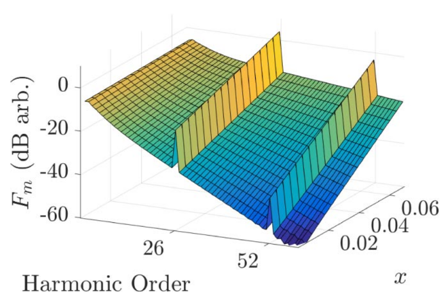

a) Analytical - Ellipses

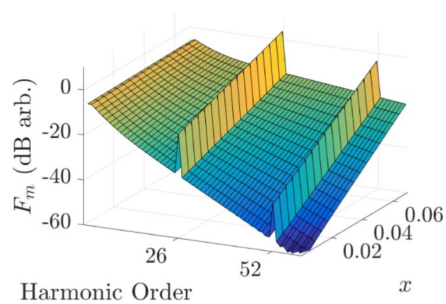

b) Analytical - Flat Plates

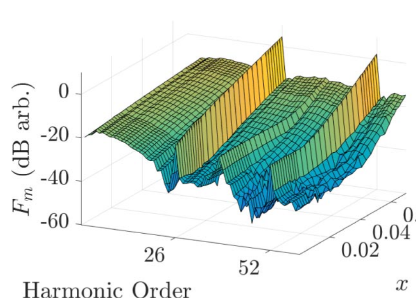

c) Numerical LBM Simulation

Fig. 8 Fourier decomposition of the upwash velocity of the potential distortion for the analytical models and the numerical results in the heterogeneous configuration ($V = 26$).

(smaller axial coordinate x). To better visualize its axial evolution, two-dimensional plots are given for some selected harmonic orders in Fig. 9a. This harmonic 38 is seen to reach a plateau at approximately ~0.7 of the dimensionless interstage coordinate. With the continuous decrease of the main harmonic 26, at the rotor leading edge, the levels of the two harmonics become comparable. Another minor harmonic of order $m = 30$ has also been plotted to illustrate that not all harmonics reach a saturation in the heterogeneous case of the high-solidity stator and to ensure that it is not a numerical artifact.

The origin of such a saturation phenomenon can be traced to a nonlinear interaction between the stator potential field and the rotor wake. A first indication is shown in Fig. 9b, where the space Fourier harmonics 38 of both the wake (rotating pattern) and the potential stator field (stationary pattern) are seen to merge at about ~0.7 of the dimensionless interstage coordinate. The order 38 is unexpected for the rotor wakes according to analytical linear theories. The latter predict the nearly exponential decrease for the potential field. In contrast, nonlinear interactions yielding saturation could be

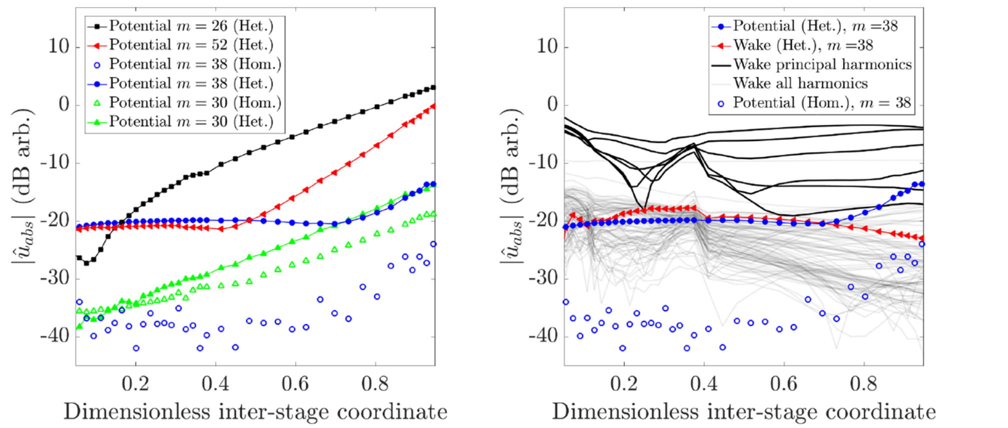

a) Potential harmonics **b) Combined wake harmonics and potential harmonic**

Fig. 9 Axial evolution of wake and potential harmonics for the vane count $V = 26$.

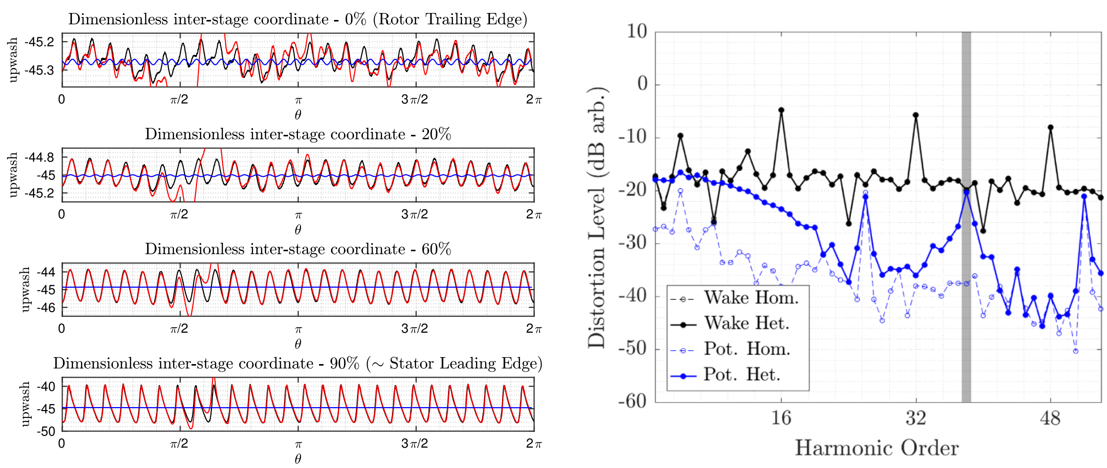

a) Upwash velocity along circumferential coordinate at several locations in the interstage **b) Wake and potential velocity harmonics at 15% of the rotor-stator distance**

Fig. 10 Wake and potential fields for the vane count $V = 26$.

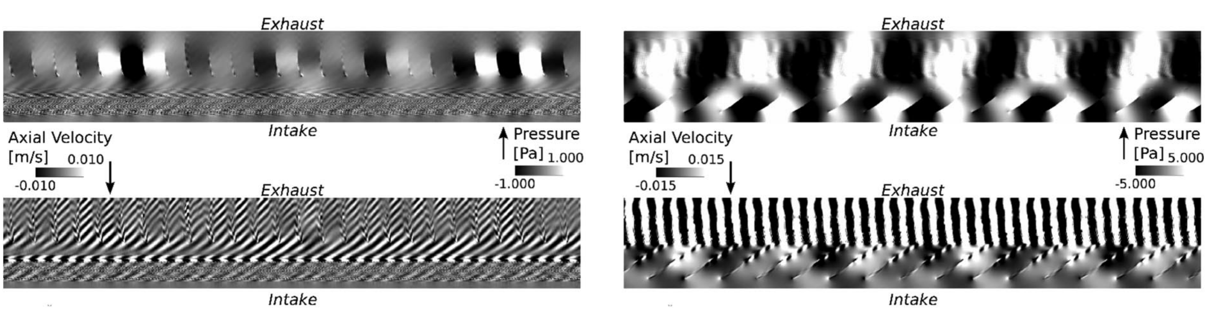

a) In the stator reference frame **b) In the rotor reference frame**

Fig. 11 Pressure and axial velocity instantaneous fields of time harmonic 38.

expected in the numerical potential field at high solidity as was found both experimentally and numerically by Parker [39]. Moreover, by looking at the axial evolution of the potential upwash velocity profiles in Fig. 10a, the modification of one vane is seen to perturb the regular profile with V lobes, to progressively interfere with the B rotor wakes, and with the decrease of the potential getting closer to the rotor, a periodic structure with 38 lobes is observed. This is further confirmed by looking at the harmonics of the wake and potential absolute velocity fields at various dimensionless interstage coordinates (at 15% of the rotor–stator distance in Fig. 10b).

The presence of the harmonic 38 is observed again in the rotor-blade unsteady loadings in Sec. IV.D, where it is also seen dominant. This particular mode structure has further been investigated by decomposing the axial-velocity and pressure fields in both the stator and rotor reference frames as Fourier time series. The time harmonic of order 38 can then be reconstructed in the two reference frames, as shown in Fig. 11. According to linear principles, the time harmonic 38 would only make sense in the rotor reference frame, and the space harmonic 38 would only be present in the stator reference frame. Yet, in the present case, both the time and space harmonics are obviously seen in both reference frames, which confirms the aforementioned coupling. In the stator reference frame, the mode is trapped in the interstage, and some acoustic resonance involving three successive vane passages can be observed in the pressure field, which can be referred to Parker's β mode (pressure peak centered at the vane midchord) weighted by some stationary-wave envelope [35]. In the rotor reference frame, a particular structure on the pressure field involving three successive blade passages can be identified, and a clear interaction with the stator vane passage can be seen. In the velocity field, lobes in the wake following the orientation of the blade are also found and are especially intense in front of locations in the stator reference frame, where the saturation of pressure was identified in Fig. 11a (top). They correspond to large coherent structures, again supporting Parker's observations that such nonlinear developing modes in rotor–stator configurations are forced by the rotor vortex-shedding structures [40].

For a more quantitative comparison of the analytical and numerical potential fields, the interpolated exponential coefficients from Eq. (16) are shown in Figs. 12 and 13 and compared with the extraction for the homogeneous case. The a_m coefficient directly determines the distortion amplitude of the gust and b_m the rate of axial decay. The numerical extraction for $V = 14$ shows identical distortion levels at the vane-number harmonics. The analytical models overestimate the numerical extractions for a_m by 5 to 15 dB at low orders. Yet the overall trend of the rate of decrease (b_m) is well captured by the two models. The analytical models predict a linear growth of the coefficient b_m with the order, which means that the distortion with higher harmonic orders will decrease faster axially. This is also consistent with Parker's findings [36]. Numerical results seem to reproduce that feature, even though errors become larger for higher orders. The broad bell-shaped hump that can be observed at low orders for the numerical results of the heterogeneous configuration is not reproduced by the analytical models. For this reason, an additional analytical model was investigated based on a Joukowski airfoil accounting for both camber and thickness effects. Higher distortion levels were observed; however, the hump at low orders was still not observed.

Finally, results are plotted for a stator of 26 vanes in Fig. 13. As previously mentioned, the harmonic $m = 38$ is found in the heterogeneous numerical case. The second harmonic order $m = 2$ V is underpredicted by the analytical models, but numerical results for a_m get closer to the analytical predictions at the lowest orders.

In all the investigated cases, the flat-plate potential theory reproduced the major characteristics of the numerical potential field accurately. This model is therefore chosen for its simplicity and its low number of parameters (stagger and chord). It is worth noting that, even in the homogeneous numerical case, because of flow distortion in the simulation induced by the filling of the laboratory and the transition from a square room to a circular bell mouth [41], all orders are generated, unlike in the ideally periodic analytical models. However, their level is lower than in the heterogeneous case and often lay close to the numerical background errors.

Finally, the surface of Fourier coefficients reconstructed from the interpolations performed for each order using the exponential fit mentioned in Sec. IV is shown in Fig. 14. The surface is quite similar to the one shown in Fig. 7c. The exponential fit is then a satisfactory approximation. It is worth noting that, for the case of harmonic saturation, the exponential rate of decrease is not captured because analytical models do not account for this nonlinear phenomenon.

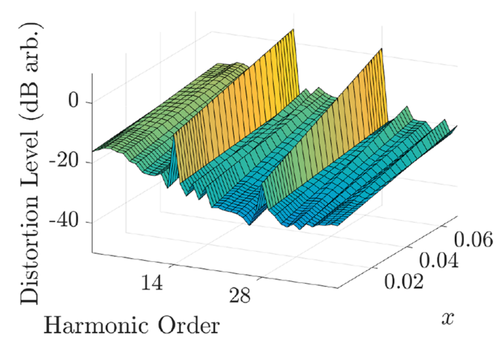

Fig. 14 Interpolated Fourier coefficients of the potential upwash velocity. Same parameters as in Fig. 7c.

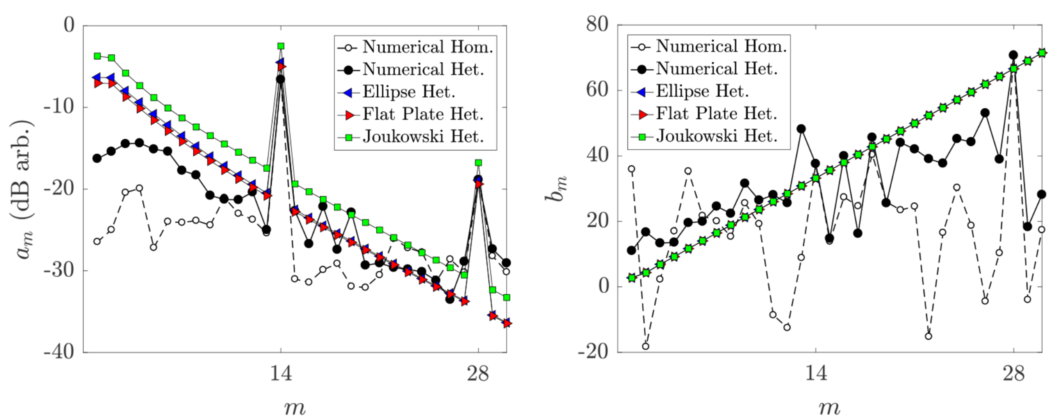

a) a_m coefficients as a function of the order **b) b_m coefficients as a function of the order**

Fig. 12 Exponential-fit parameters of the interpolated Fourier coefficients of the potential upwash velocity for $B = 16$ and $V = 14$.

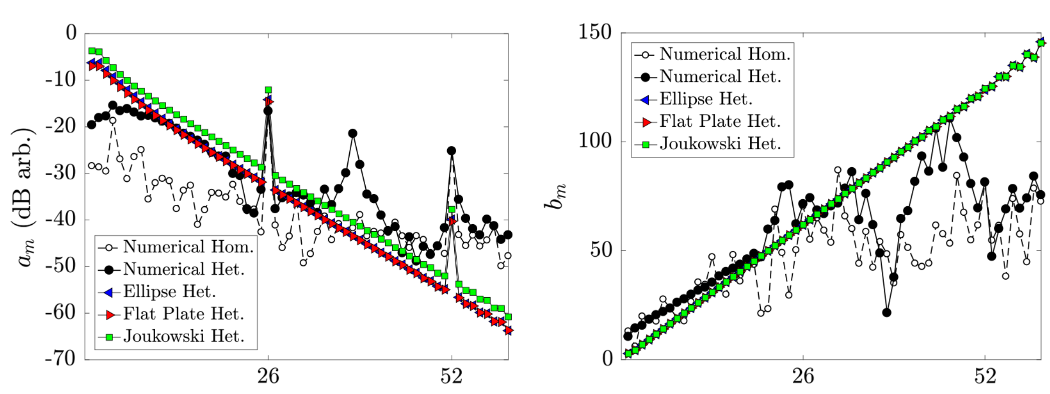

a) a_m coefficients as a function of the order **b) b_m coefficients as a function of the order**

Fig. 13 Exponential-fit parameters of the interpolated Fourier coefficients of the potential upwash velocity for $B = 16$ and $V = 26$.

D. Unsteady Blade Loading

In this section, numerical and analytical unsteady blade loadings are compared. On the one hand, the analytical unsteady lift is given by Parry's model described in Sec. III.D, choosing the flat-plate distortion for its best accuracy. On the other hand, numerical pressure jumps are calculated by a postprocessing of the unsteady numerical simulations with some approximations. To be able to compare both approaches, the numerical pressure jump must be computed at a constant radius and reduced to the one over a flat plate. The first step consists of performing a Fourier transform of the unsteady pressure over the blade surface at the rotational shaft harmonics. Then, a cylindrical cut is unwrapped to reduce the problem to two dimensions. For each isolated airfoil of the cascade, the geometrical leading and trailing edges are determined, and the upper and lower sides of the airfoil are separated. The mean camber line is approximated by the mean vertical coordinate of two points having the same dimensionless curvilinear abscissa on the upper and lower side curves. The pressure jump over the mean camber line is given by the pressure difference between both sides of same curvilinear abscissa. Finally, a simple projection of the mean camber line on the chord-line axis is done to reduce the pressure jump to that of an equivalent flat plate. A comparison of the two approaches for the $V = 14$ heterogeneous configuration is presented in Fig. 15.

The first harmonic is well approximated by the analytical model with a maximum amplitude of 12, as seen in Fig. 16. The chordwise dynamics of the loading is similar and more concentrated in the aft part of the blade, with a drop at the trailing edge, where the Kutta condition is satisfied. In Fig. 15, harmonics of lower orders due to the heterogeneity are reproduced by the analytical model but at much smaller amplitudes. The rate of decrease with the harmonic order is also far more important in the analytical model, leading to negligible lift distributions at the third, fourth, and fifth harmonics. The numerical simulation of the heterogeneous configuration includes minor inhomogeneities that are absent in the analytical model. This could make the harmonic decrease slower. Furthermore, the upstream distortion also affects the blade loading as described in Sec. IV.F. This means that the numerical pressure jump includes an additional contribution not included in the analytical result. It is worth noting that, because of its low-order azimuthal content, the inlet distortion is expected to induce low-order harmonics on the blades as observed in Fig. 15b.

In the second stator configuration ($V = 26$), the numerical pressure jumps are plotted in Fig. 17. The unexpected order $m = 38$ previously observed in Sec. IV.C is still present with the same level as the first and second harmonics. It is also noted that the unsteady lift does not decrease with increasing order. Analytical results are not plotted here because their amplitudes are negligible. In fact, when increasing the number of stator vanes, and according to the distortion field description shown in Fig. 13, loads become negligible. Thus, the high harmonic rate of decrease observed in the previous configuration is emphasized with a higher stator count, leading to a high underestimation of the unsteady lift.

To summarize, Parry's model reproduces some interesting characteristics of the unsteady lift induced by downstream potential perturbations fairly well. However, some unrealistic features such as the harmonic rate of decrease should be investigated, which are directly linked with the distortion field description.

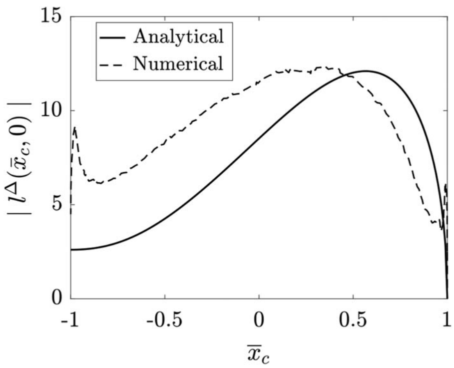

Fig. 16 Compared numerical and analytical pressure jumps at the harmonic order $m = 14$ in the heterogeneous configuration with $V = 14$.

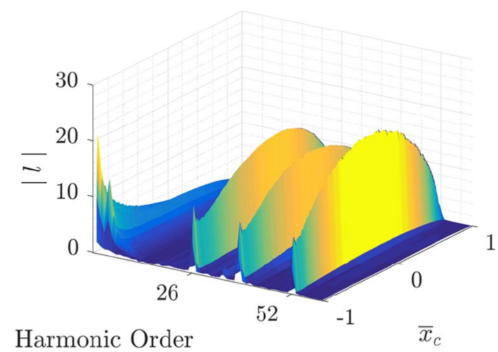

Fig. 17 Numerical rotor loads ($V = 26$).

E. Wake Interaction

From the mean field shown in Fig. 6a, the Fourier coefficients of the absolute velocity can be computed in the interstage region for several axial positions. Results for the two investigated configurations are plotted in Fig. 18. As observed by Jaron et al. [42], the first three harmonics first decrease from the blade trailing edge and then increase.

The higher vane count is also checked to only induce a minor difference in Fig. 18, mostly on the second harmonic, for which it reaches the level of the first harmonic at the stator leading edge. Finally, the heterogeneous vane does not modify the overall axial variation. In all investigated configurations, the wake-induced upwash on the vanes will be similar and could be modeled with the same parameters.

The evolution at different spanwise positions is shown in Fig. 19. The same evolution is obtained close to the hub, but near the casing, the velocity harmonics demonstrate a rapid decay after the interface between the rotor and stator domains and then a new rapid increase. The latter is related to the tip flow that merges with the wake flow.

The rotor-wake impingement will in turn induce unsteady vane loadings, which are plotted in Fig. 20 for the two different stator configurations. As expected, loads concentrate at the leading edge and decrease rapidly toward the trailing edge. The rotor periodicity emerges clearly in the plot, with the principal harmonics being those multiples of the blade number. For the stator configuration with

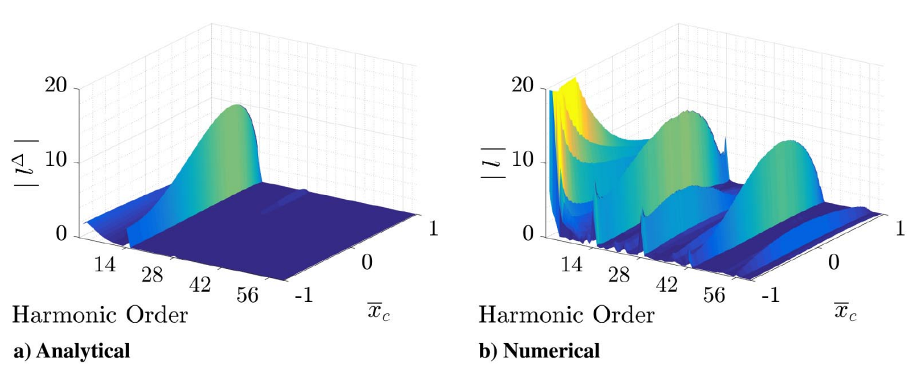

Fig. 15 Comparison of rotor blade loading harmonics as function of harmonic order and chordwise location ($V = 14$).

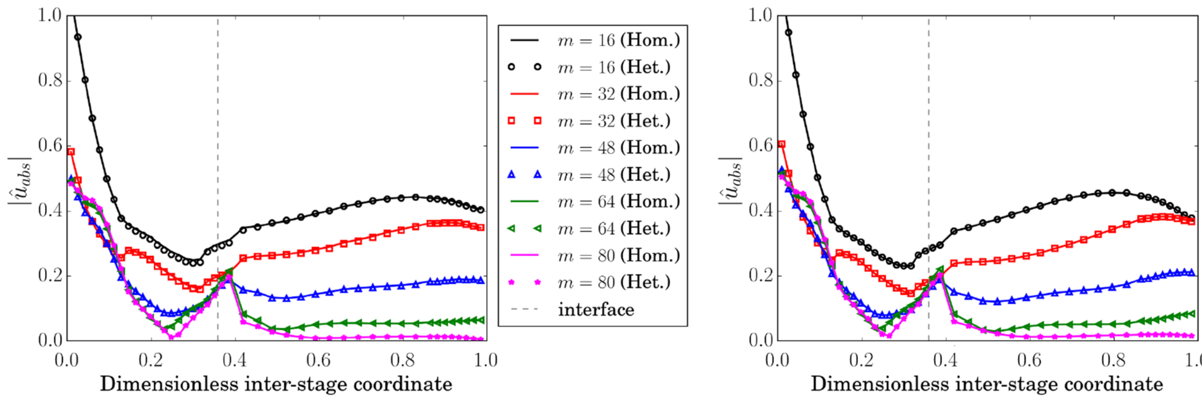

a) $V = 14$ b) $V = 26$

Fig. 18 Axial variation of the wake Fourier coefficients for the first five harmonics at midspan.

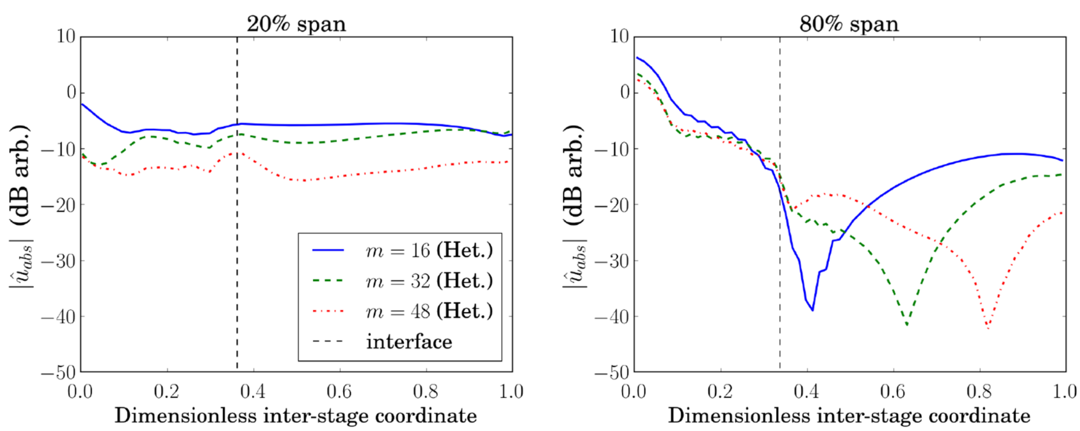

Fig. 19 Axial evolution of the first three harmonics at two other radial positions ($V = 26$ heterogeneous).

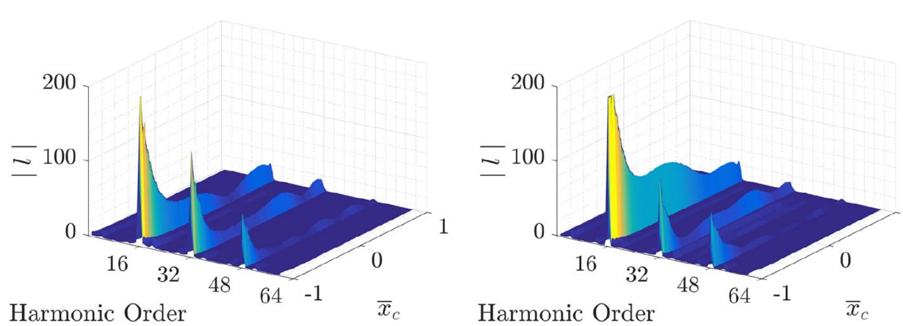

a) $V = 14$ b) $V = 26$

Fig. 20 Stator-vane loading distribution as a function of harmonic order and chordwise location for the homogeneous configurations at midspan.

26 vanes, loads can double at midchord, but the maximum value recorded at the leading edge remains the same.

Moreover, numerical loading distributions of the main harmonics $m = 16$ over the vane chord length are shown for all stator vanes in Fig. 21. In green, all vane loadings of the homogeneous configuration are superposed; in both configurations, loads are identical. Despite the geometrical difference of the modified vane, loads close to the leading edge have similar level and shape for all configurations. In fact, the homothetic transformation does not induce a major modification of the leading edge region, with the thickness of the airfoil being hardly modified. Yet, as previously mentioned, because of the higher solidity, loads at midchord are higher for the configuration with a higher stator count $V = 26$ (Fig. 21b). In the heterogeneous configuration with $V = 14$ stator vanes (Fig. 21a), stator loads also remain identical for all unmodified vanes, and the modified vane presents an extended load distribution due to its larger chord only. For the high-count heterogeneous configuration with $V = 26$ stator vanes (Fig. 21b), more variations are seen in the loadings that are about 40% higher than in the homogeneous configuration. Indeed, because the solidity is higher, the adjacent vanes (in red) are strongly perturbed by the modified vane. Finally, for all configurations, the stator-vane loads are much higher than those of the rotor blades, and the noise contribution of the wake impingement is therefore expected to be higher than the potential interaction noise.

F. Upstream Distortion

One competing mechanism of the potential interaction is the upstream distortion interaction. As previously found by Sturm et al. [41,43] with the USI-7 fan mounted in a duct in the Siegen anechoic wind tunnel, LBM simulations accounting for the full test-rig installation can capture the inflow distortion and the distortion noise mechanism accurately. The incoming flowfield is similarly resolved

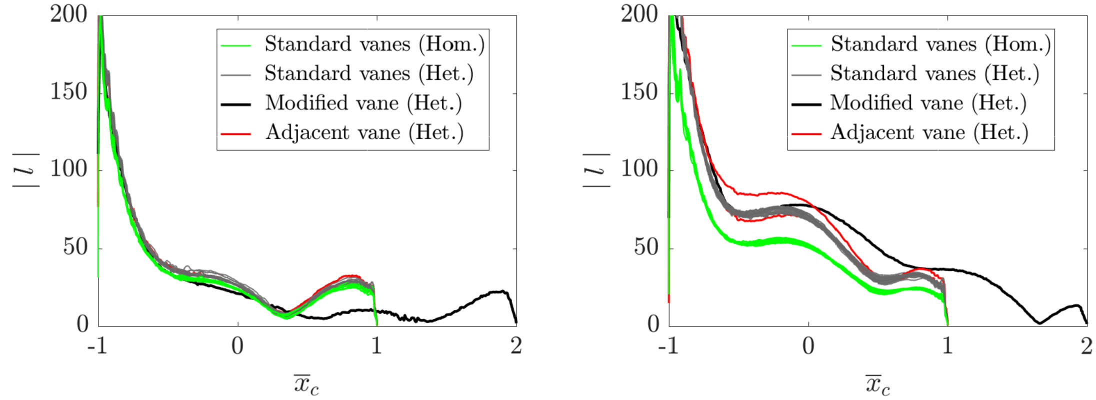

Fig. 21 Stator-vane loading distribution for the harmonic order $m = 16$ as a function of the chordwise location at midspan.

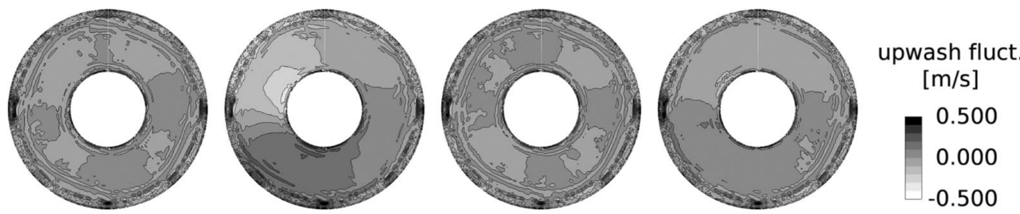

Fig. 22 Upwash velocity fluctuation seen by the rotor due to the upstream distortion.

in the present LBM simulation setup that accounts for the actual nacelle geometry and the laboratory volume. To evaluate the distortion, a time-averaged field is extracted from the simulations in the duct at $C_R/4$ upstream of the rotor-blade leading edge. The upwash velocity fluctuation seen by the rotor is shown for the four studied configurations in Fig. 22. This fluctuation is obtained by further subtracting the mean tangential field (zero azimuthal harmonic). The distortion is actually hardly noticeable in the time-averaged upwash velocity, demonstrating that the distortion is not as strong as in the USI-7 configuration and that no clear ingested vortex can be observed in the ANCF configurations. The main zones of intense azimuthal variations of the upwash velocity are the areas close to the casing and the hub as a consequence of developing boundary layers on the surface wall. All maps in Fig. 22 exhibit a four-lobe disturbance in the tip region consistent with a square to circular transition from the computational domain to the nacelle geometry. Yet, only for the homogeneous configurations, such a pattern extends over the whole blade span. In the heterogeneous cases, lower orders seem to dominate, and the distortion appears stronger for the 14-vane configurations than for the 26-vane ones.

The resulting azimuthal coefficients of the upwash velocity seen by the rotor are shown in Fig. 23 for three spanwise locations. At midspan, the amplitude of the upwash velocity is clearly increased by the heterogeneity of the configurations that involve lower harmonics, and the distortion is generally lower for the configuration with the higher vane number, consistent with the distortion maps in Fig. 22. In the latter, the distortion is higher close to the casing for all configurations. At this location, the differences between the homogeneous and heterogeneous configurations is therefore mitigated. Moreover, close to the hub and the casing, the harmonics

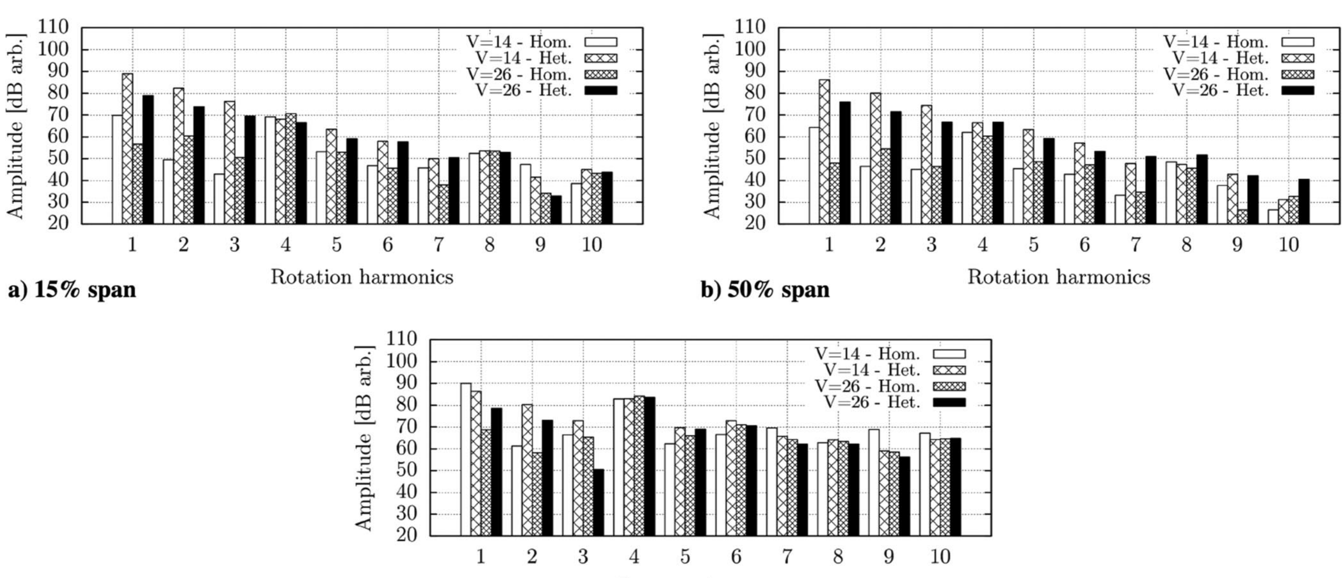

Fig. 23 Distortion Fourier coefficients of the first 10 harmonics at three span locations with arbitrary decibel scaling.

of orders $p = 4$ and $p = 8$ are noticeably higher than their neighboring harmonics, consistent with the preceding four-lobe distortion pattern. This is more clearly seen in the homogeneous configurations that do not have increased lower harmonics.

The noise from the distortion-interaction mechanism can then be estimated analytically using this upwash velocity extracted from the simulations, shown in Fig. 23. Indeed, the sound power level is calculated by Eq. (4) for a homogeneous rotor, with Amiet's flat-plate response to evaluate the unsteady lift from this leading-edge excitation.

V. Sound Predictions: Analytical Modeling Versus Lattice Boltzmann Method

A. Potential-Interaction Noise

The rotor-noise contribution due to the stator heterogeneity is investigated in this section using Parry's blade response extension computed by Eq. (13) with Goldstein's analogy given in Eqs. (3) and (4). As mentioned previously, the rotor blades are divided into 19 strips, on which the velocity perturbation from the flat-plate cascade given by Eq. (16) (modeling the stator as detailed in Sec. IV.C) is used to compute the isolated blade response given by Eqs. (11) and (12), which is then integrated over the blade span. For the four configurations, the upstream and downstream acoustic powers obtained for the first 10 blade-passing frequencies are shown in Fig. 24. With $V = 14$ vanes, the acoustic powers for the homogeneous and heterogeneous configurations are identical or show less than 2 dB differences. With $V = 26$ vanes, the BPF is cut off in the homogeneous configuration according to Tyler and Sofrin's rule (because the excitation is V-periodic) and cut on in the heterogeneous configuration. All other harmonics are of similar amplitudes with slightly higher differences than in the low-count configuration. The maximum difference is obtained for the third harmonics, with up to 5 dB differences downstream.

The detailed distribution over azimuthal orders of the first three blade-passing frequencies is given in Fig. 25. The main contribution comes from the expected Tyler and Sofrin's modes. The excitation is predominant for the loading harmonics multiples of V, as shown in

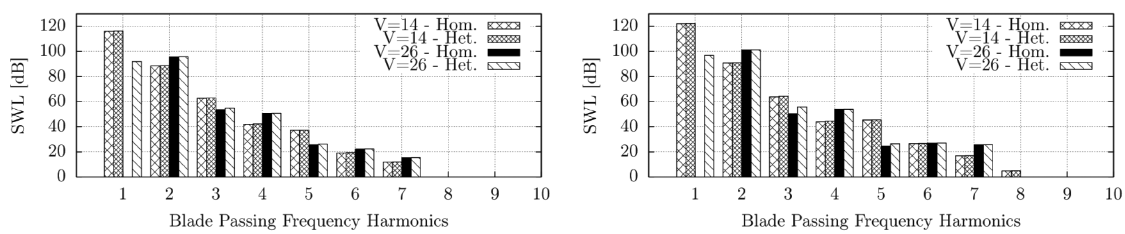

a) Upstream Acoustic Power **b) Downstream Acoustic Power**

Fig. 24 Acoustic power for the potential distortion noise of the rotor computed from Parry's flat-plate response with Goldstein's analogy.

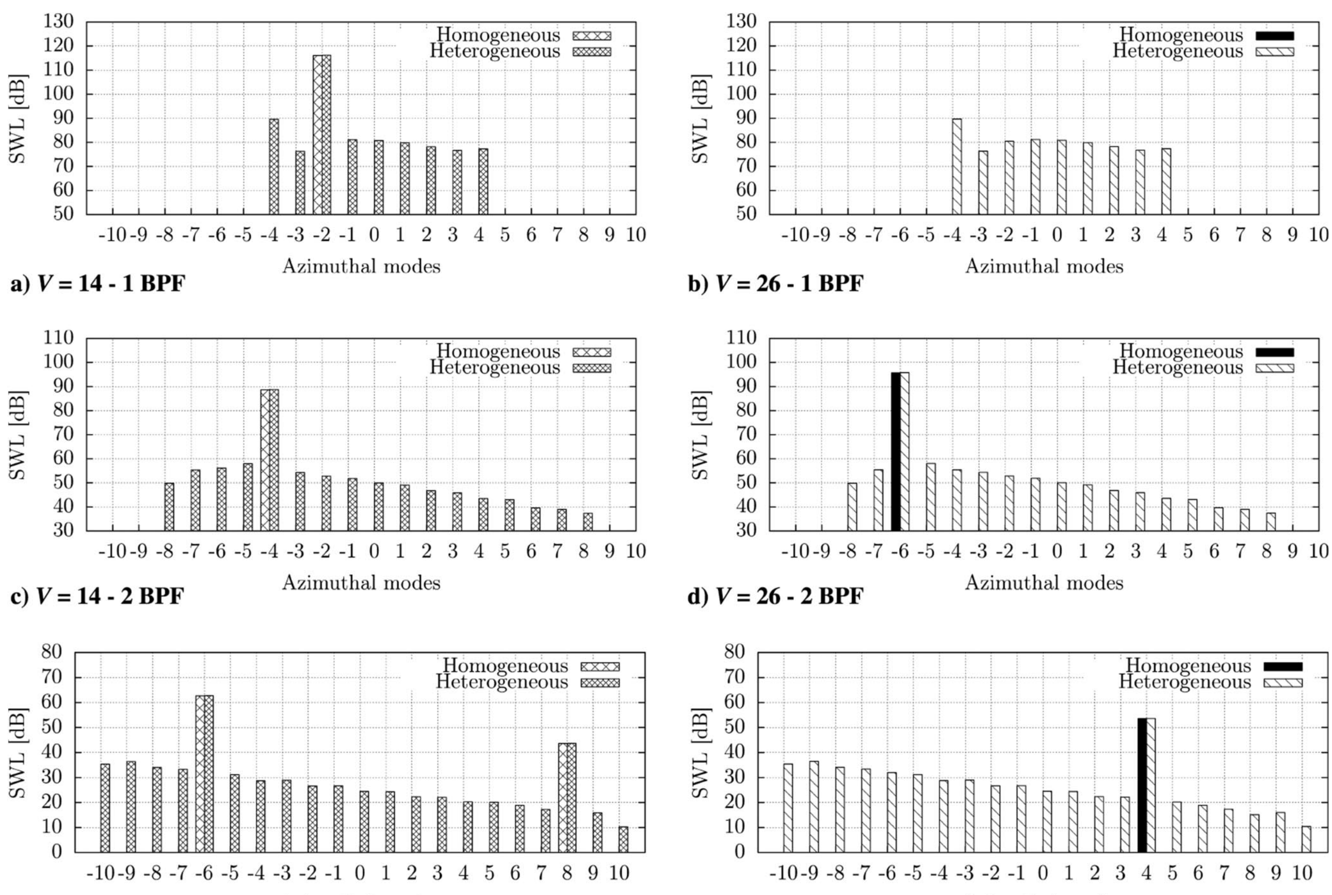

a) *V* = 14 - 1 BPF **b) *V* = 26 - 1 BPF**

c) *V* = 14 - 2 BPF **d) *V* = 26 - 2 BPF**

e) *V* = 14 - 3 BPF **f) *V* = 26 - 3 BPF**

Fig. 25 Upstream acoustic power for the potential interaction noise. Flat-plate cascade computed from Parry's response with Goldstein's analogy.

Figs. 12 and 13. In the heterogeneous configurations, the other azimuthal modes are generated but have a level at least 20 dB lower than the main radiating modes.

B. Wake-Interaction Noise

The stator-noise contribution due to the rotor-wake interactions accounting for heterogeneous vane geometry is investigated using Amiet's blade response computed by Eq. (B4) with Goldstein's analogy given in Eqs. (4) and (5). Similar to previous computations, the stator vanes are divided into 19 strips, on which the excitation from the wake analyzed in Sec. IV.E and extracted at the midsection plane between the rotor and the stator is used to compute the vane response that is then integrated over the vane span. For the four configurations, the upstream and downstream acoustic powers obtained for the same first 10 blade-passing frequencies are shown in Fig. 26. The power contribution is decreasing much more slowly than for the rotor contribution in Fig. 24, making the rotor-wake interaction the dominant noise source, except for the first BPF. This could be questioned were the fast distortion decrease in the analytical model proved to be abusive. The tone-level differences between the homogeneous and heterogeneous configurations is this time stronger with $V = 14$; the levels are about 5 dB higher for the homogeneous configuration on the first five harmonics. For the higher vane number, the amplitudes predicted in the homogeneous and heterogeneous configurations are similar for all tones, except for the first one, which is cut-off in the homogeneous configuration and cut-on in the heterogeneous configuration. Because of the increase of vane number, the configuration $V = 26$ generally produces higher noise levels than the configuration $V = 14$.

The detailed distribution over azimuthal orders of the first three blade-passing frequencies is reported in Fig. 27. As for the previous mechanism, the main contribution comes from Tyler and Sofrin's modes. The other modes are again generated by the heterogeneity but have lower amplitudes by about 20 dB, except for the first harmonics. Apart from Tyler and Sofrin's modes, the modal amplitudes are relatively constant, whereas they were found to decrease for the rotor contribution in Fig. 25.

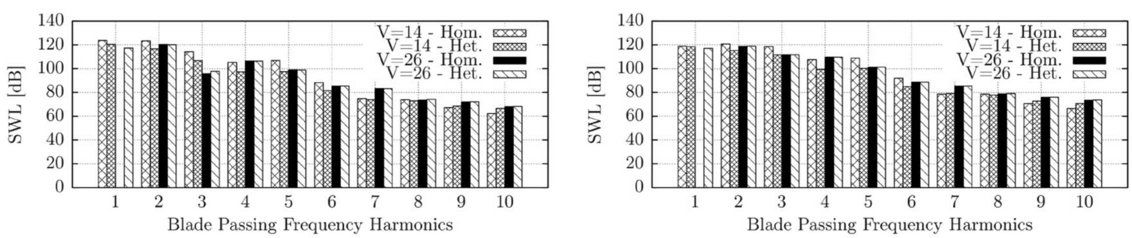

a) Upstream Acoustic Power

b) Downstream Acoustic Power

Fig. 26 Acoustic power spectra for the rotor-wake interaction noise computed from Amiet's response with Goldstein's analogy.

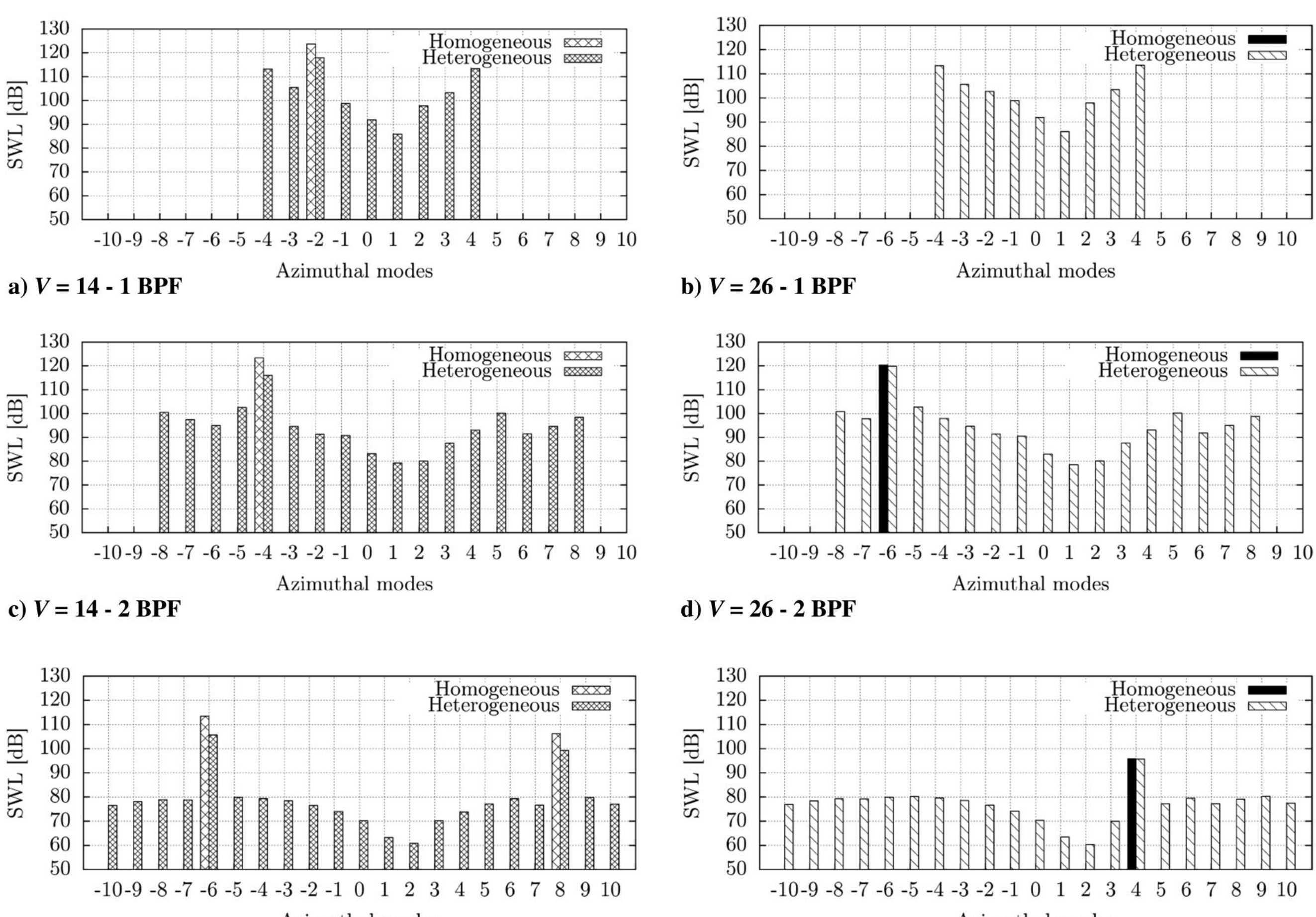

a) $V = 14$ - 1 BPF

b) $V = 26$ - 1 BPF

c) $V = 14$ - 2 BPF

d) $V = 26$ - 2 BPF

e) $V = 14$ - 3 BPF

f) $V = 26$ - 3 BPF

Fig. 27 Upstream acoustic power for the rotor-wake interaction noise computed from Amiet's response with Goldstein's analogy.

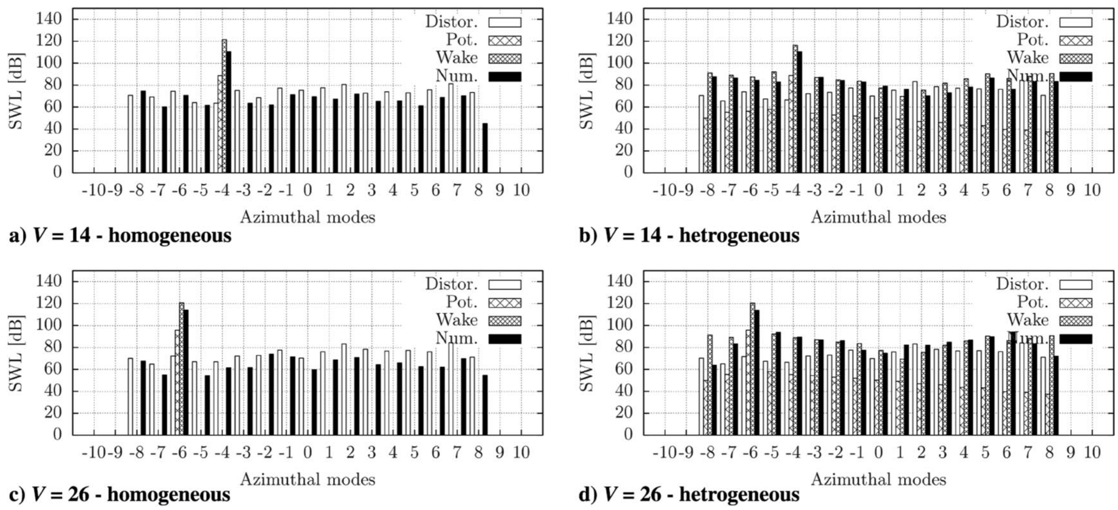

Fig. 28 Upstream modal powers of the second BPF harmonic. Comparison between numerical simulation and analytical predictions for the upstream distortion-interaction noise, the potential-interaction noise, and the wake-interaction noise.

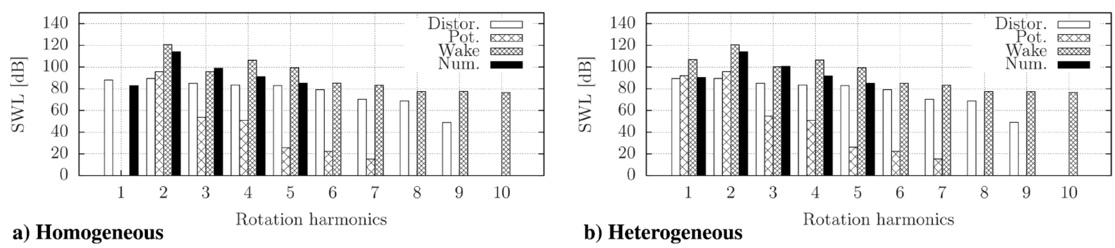

Fig. 29 Upstream acoustic power spectra for all noise mechanisms in the configuration $V = 26$.

C. Comparison with Direct Acoustic Simulations

The acoustic modal distribution is extracted from the simulation by projecting the azimuthal pressure coefficient recorded on a regular grid onto the radial shape functions of the infinite duct [11,13]. The extraction at high-frequency sampling recorded upstream of the rotor is interpolated onto a regular grid of 180×50 points in azimuthal and radial directions respectively. The Moore–Penrose pseudoinverse algorithm as implemented in Matlab is used for least-square analysis of the overdetermined system.

In Fig. 28, the modal power distribution over the azimuthal orders is shown at the second blade-passing frequency for the four configurations. The contributions from the wake-interaction noise and the potential-interaction noise according to the analytical modeling are shown separately. The wake contribution is largely prevailing. In the numerical simulations, the radiating modes appear above 60 dB, with the remaining amplitudes in the homogeneous configurations being due to the inflow distortion as clearly recovered by the analytical calculations. For heterogeneous configurations, the amplitudes of modes other than Tyler and Sofrin's modes are largely higher than the level of inflow distortion noise. This is a clear demonstration of the impact of the heterogeneity on the acoustic radiation as resolved by the simulations. Despite the increase in distortion in the heterogeneous configuration, the resulting increase in acoustic power is negligible. The acoustic power related to the effect of the stator potential field on the rotor is negligible compared with the upstream distortion contribution, as illustrated for instance for both configurations $V = 26$ in the upstream direction in Fig. 29. But it should be stressed again that the amount of potential distortion is quite moderate in the present study. The analytical prediction for the wake-interaction noise overestimates the modes detected in the simulation by 5 to 10 dB, in agreement with previous comparisons for other homogeneous configurations [13]. Nevertheless, the overall distribution and evolution of the modal spectrum for the wake interaction is in good agreement with the numerical extractions.

VI. Conclusions

Simulations using the lattice Boltzmann method as implemented in Powerflow 5.0 have been successfully performed on the baseline and modified configurations of the NASA Active Noise Control Fan (ANCF) test rig. This fan–outlet guiding vane mockup is used as a reference case typical of low-speed high-bypass-ratio engines. Four configurations have been simulated: two homogeneous with 14 and 26 identical vanes, and two heterogeneous in which a single vane of the stator is enlarged by a scale factor of 1.5. The noise originating from the potential effect induced on the rotor by the stator heterogeneity, from the upstream distortion, and from the homogeneous rotor-wake interaction with the heterogeneous stator has been investigated and compared with predictions using analytical aeroacoustic models with in-duct propagation. The classical Amiet's response for the wake impingement on the stator and the upstream distortion interaction with the rotor is used, whereas Parry's response for the impact of the potential field on the rotor row has been reformulated using Schwarzschild's technique. For the latter, the previously developed reversed Sears analytical model for the potential interaction has been extended to account for the Kutta condition at the rotor trailing edges and shown to be equivalent to Parry's approach based on the Wiener–Hopf technique. The three distinct excitations are extracted from the numerical simulations and compared with simplified analytical excitation models. The inviscid theory for two-dimensional uniform flow past flat plates is sufficient to predict the main trends of the evolution of the potential excitation seen by the rotor, and Jaron's wake model provides a good understanding of the wake evolution in the simulated configurations. The modeled potential harmonics show the same axial variations with mode order as Parker's model and measurements for all configurations. Only the saturation of some harmonics of the potential distortion attributed to nonlinear interaction between the stator potential field and the rotor wakes is missed by the proposed linear model, which is also consistent with Parker's previous experimental and numerical results. Finally, the acoustic predictions and the distribution of the acoustic modal power over the azimuthal mode orders are compared with direct acoustic information extracted from the simulation and decomposed in acoustic duct modes. The wake contribution is the dominant noise source in the present configurations. The heterogeneity strongly affects the distribution of the acoustic power on azimuthal orders by relaxing Tyler and Sofrin's rule. The analytical predictions overestimate the numerical simulations, but the relative amplitudes of the dominant and secondary modes are well captured, providing a simplified tool to estimate the acoustic levels and their distribution over modes in complex configurations. Finally, an acoustic resonance (Parker's β mode) has been evidenced in a coupled simulation for the first time.

Appendix A: In-Duct Green Function

Green's function in the time domain for an infinite annular duct can be expanded on the duct mode basis from that for the Helmholtz equation in the frequency domain using the indices n and j for the circumferential and radial modes, respectively:

$$G(\boldsymbol{x}, t|\boldsymbol{x}', \tau) = \frac{i}{4\pi} \sum_{n=-\infty}^{+\infty} \sum_{j=0}^{+\infty} \frac{E_{nj}(r') E_{nj}(r) \mathrm{e}^{in(\theta-\theta')}}{\Gamma_{nj}} \times \int_{-\infty}^{\infty} \frac{\mathrm{e}^{-i(\gamma_{nj}^{\pm}(x-x')+\omega(t-\tau))}}{\kappa_{nj}} \,\mathrm{d}\omega \tag{A1}$$

where $k_0 = \omega/c_0$, and $E_{nj}(r) = N_{nj}(\cos\tau_{nj} J_n(\chi_{nj} r) - \sin\tau_{nj} Y_n(\chi_{nj} r))$ is the duct radial function defined by Rienstra and Hirschberg [44] depending on the eigenvalue χ_{nj} and of norm $\Gamma_{nj} = 2\pi R_T^2$, where

$$\tau_{nj} = \arctan\left(\frac{J_n(\chi_{nj} R_H)}{Y_n(\chi_{nj} R_H)}\right) \tag{A2}$$

$$N_{nj} = \frac{\sqrt{2}}{2} \pi \chi_{nj} R_T \left(\frac{1 - n^2/(\chi_{nj}^2 R_T^2)}{J_n(\chi_{nj} R_T)^2 + Y_n(\chi_{nj} R_T)^2} - \frac{1 - n^2/(\chi_{nj}^2 R_H^2)}{J_n(\chi_{nj} R_H)^2 + Y_n(\chi_{nj} R_H)^2} \right)^{-1} \tag{A3}$$

$\gamma_{nj}^{\pm} = (M_a k_0 \pm \kappa_{nj})/\beta^2$ is the axial acoustic wave number, and $\kappa_{nj}^2 = k_0^2 - \beta^2 \chi_{nj}^2$. The superscript $\pm$ is related to the direction of propagation for $x > x_0$ and $x < x_0$, respectively. x_0 is the position of the source plane.

Appendix B: Amiet's Blade Response

For low frequencies such that $\overline{\mu} < 0.4$, the normalized pressure jump follows Sears's compressible response:

$$g^{\star}(\overline{x}_c, \overline{k}_x, 0, M) = \frac{1}{\pi\beta} \sqrt{\frac{1 - \overline{x}_c}{1 + \overline{x}_c}} \mathcal{S}^{\star}\left(\frac{\overline{k}_x}{\beta^2}\right) \mathrm{e}^{-i(\overline{k}_x/\beta^2)(M^2 \overline{x}_c + f(M))} \tag{B1}$$

where $f(M) = (1-\beta)\ln M + \beta \ln(1+\beta) - \ln 2$, and the complex conjugate of Sears's function defined as

$$\mathcal{S}^{\star}(X) = \frac{2}{\pi X[(J_0(X) - Y_1(X)) - i(J_1(X) + Y_0(X))]} \tag{B2}$$

At higher frequencies for which the chord is not compact, Amiet's response [27] is used instead:

$$g^{\star}(\overline{x}_c, \overline{k}_x, 0, M) = \frac{\mathrm{e}^{i(\pi/4)} \mathrm{e}^{i\overline{\mu}(1-M)(1-\overline{x}_c) - \overline{k}_x}}{\pi \sqrt{2\pi(1+M)\overline{k}_x}} \times \left(\sqrt{\frac{2}{1+\overline{x}_c}} - 1 + (1-i) E(2\overline{\mu}(1-\overline{x}_c)) \right) \tag{B3}$$

The chordwise integral

$$\mathcal{L} = \int_{-1}^{1} \mathrm{e}^{-i\mathcal{B}\overline{x}_c} l(\overline{x}_c) \,\mathrm{d}\overline{x}_c$$

with $\mathcal{B} = b(\gamma_{nj}^{\pm} \cos\chi - (n/r') \sin\chi)$ for Amiet's response is given as

$$\mathcal{L} = 2\pi\rho_0 U w_0 (I_1 + I_2) \tag{B4}$$

with:

$$I_1 = \frac{2\mathrm{e}^{i\Theta_2}}{\pi\sqrt{(1+M)\overline{k}_x}} ES(2\Theta_1) \tag{B5}$$

$$I_2 = \frac{2\mathrm{e}^{i\Theta_2}}{\pi\Theta_1 \sqrt{2\pi(1+M)\overline{k}_x}} \left\{ i(1 - \mathrm{e}^{-i2\Theta_1}) + i(1-i)[\sqrt{4\overline{\mu}}\mathrm{e}^{-i2\Theta_1} Es(2(\overline{\mu}(1+M) + \mathcal{B})) - E(4\overline{\mu})] \right\} \tag{B6}$$

where $\Theta_1 = \mathcal{B} - \overline{\mu}(1-M)$, and $\Theta_2 = \mathcal{B} - \overline{k}_x + (\pi/4)$. The functions ES and ES that are providing stable computations with complex arguments [32] are related to the complex error function $\Phi^{(0)}$ as

$$ES(z) = \frac{E^{\star}(z)}{\sqrt{z}} = \frac{1-i}{2} \frac{\Phi^{(0)}(\sqrt{iz})}{\sqrt{z}}$$
$$Es(z) = \frac{E(z)}{\sqrt{z}} = \frac{1+i}{2} \frac{\Phi^{(0)}(\sqrt{-iz})}{\sqrt{z}} \tag{B7}$$

Acknowledgments

The authors acknowledge the Réseau Québécois de Calcul de Haute Performance/Compute Canada for providing technical support and necessary computational resources for this research as well as the Exa Corporation for providing licenses and technical support. The authors also thank A. Mann and F. Pérot from Exa for fruitful discussions and technical support and for providing the initial simulation. This research was funded through the Aeroacoustic Industrial Chair of the Université de Sherbrooke and the ANR Industrial Chair ADOPSYS.

References

[1] de Laborderie, J., Moreau, S., Berry, A., and Posson, H., "Several Technological Effects on Tonal Fan Noise Prediction," *18th AIAA/CEAS Aeroacoustics Conference*, AIAA Paper 2012-2131, June 2012.

[2] de Laborderie, J., and Moreau, S., "Evaluation of a Cascade-Based Acoustic Model for Fan Tonal Noise Prediction," *AIAA Journal*, Vol. 52, No. 12, 2014, pp. 2877–2890. doi:10.2514/1.J053008

[3] de Laborderie, J., Blandeau, V., Node-Langlois, T., and Moreau, S., "Extension of a Fan Tonal Noise Cascade Model for Camber Effects," *AIAA Journal*, Vol. 53, No. 4, 2015, pp. 863–876. doi:10.2514/1.J053266

[4] Holewa, A., Weckmüller, C., and Guérin, S., "Impact of Bypass-Duct Bifurcations on Fan Noise," *18th AIAA/CEAS Aeroacoustics Conference*, AIAA Paper 2012-2129, June 2012.

[5] Bonneau, V., Polacsek, C., Barrier, R., Lewy, S., Roux, J.-M., and Gervais, Y., "Tonal Noise Prediction of a Turbofan with Heterogeneous Stator and Bifurcations," *AIAA Journal*, Vol. 53, No. 11, 2015,

pp. 3354–3369.
doi:10.2514/1.J053970

[6] Daroukh, M., Moreau, S., Gourdain, N., Boussuge, J., and Sensiau, C., "Influence of Distortion on Fan Tonal Noise," *22th AIAA/CEAS Aeroacoustics Conference*, AIAA Paper 2016-2818, 2016.

[7] Sutliff, D. L., Heidelberg, L. J., Elliott, D. M., and Nallasamy, M., "Baseline Acoustic Levels of the NASA Active Noise Control Fan Rig," *2nd AIAA/CEAS Aeroacoustics Conference*, AIAA Paper 1996-1745, May 1996.

[8] Heidelberg, L. J., Hall, D. G., Bridges, J. E., and Nallasamy, M., "A Unique Ducted Fan Test Bed for Active Noise Control and Aeroacoustics Research," *2nd AIAA/CEAS Aeroacoustics Conference*, AIAA Paper 1996-1740, May 1996.

[9] McAllister, J., Loew, R. A., Lauer, J. T., and Sutliff, D. L., "The Advanced Noise Control Fan Baseline Measurements," *47th Aerospace Science Meeting*, AIAA Paper 2009-0624, Jan. 2009.

[10] Pasco, Y., Guedeney, T., Leung-Tak, A., Berry, A., Moreau, S., and Masson, P., "Active Noise Control Simulation of Tonal Turbofan Noise in Aero Engines," *20th AIAA/CEAS Aeroacoustics Conference*, AIAA Paper 2014-3187, 2014.

[11] Mann, A., Pérot, F., Kim, M.-S., Casalino, D., and Fares, E., "Advanced Noise Control Fan Direct Aeroacoustics Predictions Using a Lattice-Boltzmann Method," *18th AIAA/CEAS Aeroacoustics Conference*, AIAA Paper 2012-2287, June 2012.

[12] Maldonado, A. L. P., Miserda, R. F. B., and Pimenta, B. G., "Computational Tonal Noise Prediction for the Advanced Noise Control Fan," *18th AIAA/CEAS Aeroacoustics Conference*, AIAA Paper 2012-2128, June 2012.

[13] Sanjose, M., Daroukh, M., de Laborderie, J., Moreau, S., and Mann, A., "Tonal Noise Prediction and Validation on the ANCF Rotor–Stator Conuration," *Noise Control Engineering Journal*, Vol. 63, No. 6, 2015, pp. 552–562.
doi:10.3397/1/376349

[14] Frisch, U., D'Humiéres, D., Hasslacher, B., Lallemend, P., Pomeau, Y., and Rivet, J.-P., "Lattice Gas Hydrodynamics in Two and Three Dimensions," *Complex Systems*, Vol. 1, No. 4, 1987, pp. 649–707.

[15] Chen, S., and Dooler, G. D., "Lattice Boltzmann Method for Fluid Flows," *Annual Review of Fluid Mechanics*, Vol. 30, 1998, pp. 329–364.
doi:10.1146/annurev.fluid.30.1.329

[16] Marié, S., Ricot, D., and Sagaut, P., "Comparison Between Lattice Boltzmann Method and Navier–Stokes High Order Schemes for Computational Aeroacoustics," *Journal of Computational Physics*, Vol. 228, No. 4, 2009, pp. 1056–1070.
doi:10.1016/j.jcp.2008.10.021

[17] Vergnault, E., Malaspinas, O., and Sagaut, P., "A lattice Boltzmann Method for Nonlinear Disturbances Around an Arbitrary Base Flow," *Journal of Computational Physics*, Vol. 231, No. 24, 2012, pp. 8070–8082.
doi:10.1016/j.jcp.2012.07.021

[18] Chen, H., Orszag, S. A., Staroselsky, I., and Succi, S., "Expanded Analogy Between Boltzmann Kinetic Theory of Fluids and Turbulence," *Journal of Fluid Mechanics*, Vol. 519, Nov. 2004, pp. 301–314.
doi:10.1017/S0022112004001211

[19] Chen, H., Teixeira, C., and Molvig, K., "Realization of Fluid Boundary Conditions via Discrete Boltzmann Dynamics," *International Journal of Modern Physics C*, Vol. 9, No. 8, 1998, pp. 1281–1292.
doi:10.1142/S0129183198001151

[20] Zhang, R., Sun, C., Li, Y., Satti, R., Shock, R., Hoch, J., and Chen, H., "Lattice Boltzmann Approach for Local Reference Frames," *Communications in Computational Physics*, Vol. 9, No. 5, 2011, pp. 1193–1205.
doi:10.4208/cicp.021109.111110s

[21] Masson, V., Posson, H., Sanjose, M., Moreau, S., and Roger, M., "Fan-OGV Interaction Broadband Noise Prediction in a Rigid Annular Duct with Swirling and Sheared Mean Flow," *22th AIAA/CEAS Aeroacoustics Conference*, AIAA Paper 2016-2944, 2016.

[22] Goldstein, M. E., *Aeroacoustics*, McGraw–Hill, New York, 1976, Chap. 4.

[23] Cantrell, R. H., and Hart, R. W., "Interaction Between Sound and Flow in Acoustic Cavities: Mass, Momentum, and Energy Considerations," *Journal of the Acoustical Society of America*, Vol. 36, No. 4, 1964, pp. 697–706.
doi:10.1121/1.1919047

[24] Morfey, C. L., "Acoustic Energy in Non-Uniform Flows," *Journal of Sound and Vibration*, Vol. 14, No. 2, 1971, pp. 159–170.
doi:10.1016/0022-460X(71)90381-6

[25] Tyler, J. M., and Sofrin, T. G., "Axial Flow Compressor Noise Studies," *Society of Automotive Engineers Transactions*, Vol. 70, 1962, pp. 309–332.

[26] de Laborderie, J., "Approches Analytiques et Numériques Pour la Prédiction du Bruit Tonal et Large Bande de Soufflantes de Turboréacteurs," Ph.D. Thesis, Université de Sherbrooke, Sherbrooke, QC, Canada, 2013.

[27] Amiet, R. K., "Noise Produced by Turbulent Flow into a Rotor: Theory Manual for Noise Calculation," NASA CR-181788, 1989.

[28] Roger, M., Moreau, S., and Guédel, A., "Vortex-Shedding Noise and Potential-Interaction Noise Modeling by a Reversed Sears' Problem," *12th AIAA/CEAS Aeroacoustics Conference and Exhibit*, AIAA Paper 2006-2607, 2006.

[29] Parry, A. B., "Theoretical Prediction of Counter-Rotating Propeller Noise," Ph.D. Thesis, University of Leeds, Leeds, England, U.K., 1988.

[30] Amiet, R. K., "Acoustic Radiation from an Airfoil in a Turbulent Stream," *Journal of Sound and Vibration*, Vol. 41, No. 4, 1975, pp. 407–420.
doi:10.1016/S0022-460X(75)80105-2

[31] Amiet, R. K., "Noise Due to Turbulent Flow Past a Trailing-Edge," *Journal of Sound and Vibration*, Vol. 47, No. 3, 1976, pp. 387–393.
doi:10.1016/0022-460X(76)90948-2

[32] Roger, M., and Moreau, S., "Addendum to the Back-Scattering Correction of Amiet's Trailing-Edge Noise Model," *Journal of Sound and Vibration*, Vol. 331, No. 24, 2012, pp. 5383–5385.
doi:10.1016/j.jsv.2012.06.019

[33] Roger, M., François, B., and Moreau, S., "Cascade Trailing-Edge Noise Modeling Using a Mode-Matching Technique and the Edge-Dipole Theory," *Journal of Sound and Vibration*, Vol. 382, 2016, pp. 310–327.
doi:10.1016/j.jsv.2016.06.035

[34] Panton, R. L., *Incompressible Flow*, Wiley, Hoboken, NJ, 2013, Chap. 18.

[35] Parker, R., "Resonant Effects in Wake Shedding from Parallel Plates: Calculation of Resonant Frequencies," *Journal of Sound and Vibration*, Vol. 5, No. 2, 1967, pp. 330–343.
doi:10.1016/0022-460X(67)90113-7

[36] Parker, R., "Relation Between Blade Row Spacing and Potential Flow Interaction Effects in Turbomachines," *Proceedings of the Institution of Mechanical Engineers*, Vol. 184, No. 7, 1969, pp. 1–8.

[37] Gomar, A., , and Léonard, T., et al., "Antares: Python Post-Processing Library," 2012, http://www.cerfacs.fr/antares/, 2012. CERFACS.

[38] Guedeney, T., and Moreau, S., "Unsteady RANS Simulations of a Low Speed Fan for Analytical Tonal Noise Prediction," *11th European Turbomachinery Conference*, Madrid, 2015.

[39] Parker, R., "Pressure Fluctuations Due to Interaction Between Blade Rows in Axial Flow Compressors," *Proceedings of the Institution of Mechanical Engineers*, Vol. 183, No. 1, 1968, pp. 153–164.
doi:10.1243/PIME_PROC_1968_183_016_02

[40] Parker, R., "Resonance Effects in Wake Shedding from Compressor Blading," *Journal of Sound and Vibration*, Vol. 6, No. 3, 1967, pp. 302–309.
doi:10.1016/0022-460X(67)90202-7

[41] Sturm, M., Sanjose, M., Moreau, S., and Carolus, T., "Aeroacoustic Simulation of an Axial Fan Including the Full Test Rig by Using the Lattice Boltzmann Method," *FAN 2015, International Conference on Fan Noise, Technology and Numerical Methods*, Lyon, France, 2015.

[42] Jaron, R., Moreau, A., and Guerin, S., "RANS-Informed Fan Noise Prediction: Separation and Extrapolation of Rotor Wake and Potential Field," *20th AIAA/CEAS Aeroacoustics Conference*, AIAA Paper 2014-2946, 2014.
doi:10.2514/6.2014-2946

[43] Sturm, M., Sanjose, M., Moreau, S., and Carolus, T., "Application of Analytical Noise Models using Numerical and Experimental Fan Data," *11th European Conference on Turbomachinery Fluid Dynamics and Thermodynamics*, Madrid, 2015.

[44] Rienstra, S. W., and Hirschberg, A., *An Introduction to Acoustics*, Eindhoven Univ. of Technology, 2004, Chap. 7, https://www.win.tue.nl/~sjoerdr/papers/boek.pdf.

C. Bailly
Associate Editor